

Testing the cosmological principle with the Pantheon+ sample and the region-fitting method

J. P. Hu¹, Y. Y. Wang², J. Hu³, and F. Y. Wang^{1,4}

¹ School of Astronomy and Space Science, Nanjing University, Nanjing 210093, China
e-mail: fayinwang@nju.edu.cn

² Anton Pannekoek Institute for Astronomy, University of Amsterdam, Science Park 904, 1098 XH Amsterdam, Netherlands

³ Institute of Astronomy and Information, Dali University, Dali 671003, China

⁴ Key Laboratory of Modern Astronomy and Astrophysics (Nanjing University), Ministry of Education, Nanjing 210093, China

Received date; accepted date

ABSTRACT

The cosmological principle is fundamental to the standard cosmological model. It assumes that the Universe is homogeneous and isotropic on very large scales. As the basic assumption, it must stand the test of various observations. In this work, we investigated the properties of the Pantheon+ sample, including redshift distribution and position distribution, and we give its constraint on the flat Λ CDM model: $\Omega_m = 0.36 \pm 0.02$ and $H_0 = 72.83 \pm 0.23 \text{ km s}^{-1} \text{ Mpc}^{-1}$. Then, using the region fitting (RF) method, we mapped the all-sky distribution of cosmological parameters (Ω_m and H_0) and find that the distribution significantly deviates from isotropy. A local matter underdensity region exists toward $(308.4^{+47.6}_{-48.7}, -18.2^{+21.1}_{-28.8})$ as well as a preferred direction of the cosmic anisotropy $(313.4^{+19.6}_{-18.2}, -16.8^{+11.1}_{-10.7})$ in galactic coordinates. Similar directions may imply that local matter density might be responsible for the anisotropy of the accelerated expansion of the Universe. Results of statistical isotropy analyses including Isotropy and Isotropy with real-data positions (RP) show high confidence levels. For the local matter underdensity, the statistical significances are 2.78σ (isotropy) and 2.34σ (isotropy RP). For the cosmic anisotropy, the statistical significances are 3.96σ (isotropy) and 3.15σ (isotropy RP). The comparison of these two kinds of statistical isotropy analyses suggests that inhomogeneous spatial distribution of real sample can increase the deviation from isotropy. The similar results and findings are also found from reanalyses of the low-redshift sample (lp+) and the lower screening angle ($\theta_{\max} = 60^\circ$), but with a slight decrease in statistical significance. Overall, our results provide clear indications for a possible cosmic anisotropy. This possibility must be taken seriously. Further testing is needed to better understand this signal.

Key words. cosmology: theory – cosmological parameters – supernovae: general

1. Introduction

The Λ CDM model is generally accepted as the standard cosmological model, which is consistent with most astronomical observations (Scolnic et al. 2018; Abbott et al. 2019; Khadka & Ratra 2020; Brout et al. 2022; Cao & Ratra 2022; Dainotti et al. 2022b; Jia et al. 2022; Liu et al. 2022a; Porredon et al. 2022; Wang et al. 2022; de Cruz Pérez et al. 2023; Khadka et al. 2023; Li et al. 2023b). It is based on the fundamental assumption of the cosmological principle, namely that the Universe is statistically isotropic and homogeneous on sufficiently large scales. Despite its many successes, there have been also several analyses of observations that indicate that the Universe may be inhomogeneous and anisotropic; for instance, the fine-structure constant (Webb et al. 2011; King et al. 2012; Li & Lin 2017; Milaković et al. 2022), the direct measurement of the Hubble parameter (Bonvin et al. 2006; Kocsbang 2021), the cosmic microwave background (CMB) (Bennett et al. 2003; Tegmark et al. 2003; Bielewicz et al. 2004; Bennett et al. 2011; Gruppuso et al. 2011; Ghosh & Jain 2020; Planck Collaboration et al. 2020c), the anisotropic dark energy (Koivisto & Mota 2008; Mariano & Perivolaropoulos 2012; Bayron Orjuela-Quintana et al. 2020; Motoa-Manzano et al. 2021), the large dipole of radio source counts (Rubart et al. 2014; Colin et al. 2017; Rameez et al. 2018; Singal 2019, 2023),

quasar dipoles (Hutsemékers et al. 2005; Pelgrims & Hutsemékers 2016; Tiwari & Jain 2019; Hu et al. 2020; Secrest et al. 2021; Zhao & Xia 2021a,b; Dam et al. 2023), the anisotropic Hubble constant (Luongo et al. 2022; McConville & Colgáin 2023) and the type Ia supernovae (SNe Ia) dipole (Colin et al. 2011; Yang et al. 2014; Javanmardi et al. 2015; Sun & Wang 2018; Wang & Wang 2018; Tang et al. 2023), and local matter underdensity (Kazantzidis & Perivolaropoulos 2020). These analyses hint that the Universe may have a local void and a preferred expanding direction. In addition, it is assumed that the Λ CDM model also triggers a serious Hubble constant discrepancy between the *Planck* CMB (Planck Collaboration et al. 2020b) and the local distance ladder (Riess et al. 2019, 2022). This is known as the Hubble tension, and its statistical significance has reached 5.0σ . Such a high confidence level could not be explained by systematic uncertainty alone, and might imply new physics beyond the Λ CDM model. There has been intense discussion focused on this issue, and a lot of theoretical explanations have been proposed. We refer the readers to some review articles (Di Valentino et al. 2021; Shah et al. 2021; Abdalla et al. 2022; Perivolaropoulos & Skara 2022; Hu & Wang 2023; Kumar Aluri et al. 2023; Kroupa et al. 2023; Riess & Breuval 2023; Vagnozzi 2023) for

more detailed information about the cosmological anomalies and tension.

It is worth noting that some researchers claim that considering a void model can successfully explain the cosmic dipole and the Hubble tension (Böhringer et al. 2020; Haslbauer et al. 2020; Luković et al. 2020; Camarena et al. 2022; Cai et al. 2022; Mohammadi et al. 2023). Haslbauer et al. (2020) showed that the KBC void (Keenan et al. 2013) could naturally resolve the Hubble tension in Milgromian dynamics for the first time. By computing the Hubble constant in an inhomogeneous universe and adopting model selection via both the Bayes factor and the Akaike information criterion, Camarena et al. (2022) found that the lambda Lemaître-Tolman-Bondi (ΛLTB) model is favored with respect to the ΛCDM model at low-redshift range ($0.023 < z < 0.15$), and this can be used to explain the Hubble tension. After that, Cai et al. (2022) proposed that a gigaparsec-scale void can reconcile the CMB and quasar dipolar tension. If considering a large and thick void, their setup can also ease the Hubble tension. At the same time, there are some findings that could be explained by a local void model. For example, inspired by the H0LiCOW results (Millon et al. 2020; Wong et al. 2020), Hu & Wang (2022b) reported a late-time transition of H_0 , that is, H_0 changes from being consistent with the CMB result to being consistent with the distance ladder one from an early-to-late cosmic time, which can be explicated by the local void. The late-time transition of H_0 was found from the observational Hubble parameter $H(z)$ data combining the Gaussian process (GP) method (Pedregosa et al. 2011) and can be used to effectively relieve the Hubble tension (a mitigation level of around 70%). In addition, a similar H_0 descending behavior has also been discovered by utilizing various observations (such as SNe Ia, $H(z)$, baryon acoustic oscillations and megamasers) and their combinations (Krishnan et al. 2020, 2021b; Dainotti et al. 2022a; Ó Colgáin et al. 2022; Horstmann et al. 2022; Colgáin et al. 2022; Jia et al. 2023; Malekjani et al. 2023). Of course, there are also some opposing voices believing that the void model alone cannot solve the Hubble tension (Kenworthy et al. 2019; Cai et al. 2021; Castello et al. 2022). Therefore, further research on this controversial topic is necessary and would certainly be worthwhile. So far, there has been no research using the Pantheon+ sample to simultaneously map matter-density (Ω_m) distribution and the Hubble expansion (H_0) distribution to test the cosmological principle.

In this work, we tested the cosmological principle by the region fitting (RF) method with the latest Pantheon+ sample. Compared to the previous work (Krishnan et al. 2021a, 2022; McConville & Colgáin 2023), we improved our research methodology and carried out the necessary statistical analyses. Usually, considering the simple flat ΛCDM model, Ω_m and H_0 are considered to be negatively correlated. Therefore, for the convenience of analysis, one parameter is usually fixed. For example, some recent works fix Ω_m to 0.30 and regard H_0 as a free parameter (Krishnan et al. 2021a, 2022; McConville & Colgáin 2023). In our fitting calculation process, all cosmological parameters (Ω_m and H_0) are free to investigate the local properties of our Universe. We would like to plot the all-sky distributions of Ω_m and H_0 to find out the local matter underdensity region and the preferred direction of expansion (cosmic anisotropy), respectively. The influence of redshift and the screening angle θ_{\max} on the final results is also considered. We found the suitable angle of the RF method for the Pantheon+ sample. Then, we analysed a combination of the local void (Enqvist 2008; Garcia-Bellido & Haugbølle 2008; Keenan et al. 2013; Wang & Dai 2013; Hwang et al. 2016; Hamaus et al. 2022; Shim et al. 2023), cosmic anisotropy (Sun & Wang 2019; Akarsu et al. 2020; Migkas et al. 2020,

2021; Akarsu et al. 2022; Horstmann et al. 2022; Rahman et al. 2022; Akarsu et al. 2023; Dhawan et al. 2023; Ebrahimian et al. 2023), and Hubble tension (Chen 2019; Riess et al. 2019; Verde et al. 2019; Planck Collaboration et al. 2020b; Riess 2020; Riess et al. 2022; Capozziello et al. 2023) in detail. Finally, we compared our results with those of previous similar research (Antonioni & Perivolaropoulos 2010; Cai & Tuo 2012; Kalus et al. 2013; Wang & Wang 2014; Yang et al. 2014; Chang & Lin 2015; Lin et al. 2016b; Chang & Zhou 2019; Hu et al. 2020; Luongo et al. 2022; McConville & Colgáin 2023) and other observations, including the CMB dipole (Planck Collaboration et al. 2016, 2020a), dark flow (Abdalla et al. 2022), bulk flow (Turnbull et al. 2012; Feix et al. 2017; Watkins et al. 2023), and galaxy cluster (Migkas et al. 2021).

The outline of this paper is as follows. In Sect. 2, we give a detailed description of the Pantheon+ sample, including redshift distribution, location distribution, and corresponding density contour, and compare it to the Pantheon sample. Section 3 briefly introduces the RF method, which we used to map the all-sky distribution of cosmological parameters. In Sect. 4, we present the results from the whole and low-redshift Pantheon+ sample ($z < 0.30$, lp+) and discuss the impact of RF method with different screening angles θ_{\max} on the final results from the Pantheon+ sample. The corresponding investigation and discussion are given in Sect. 5. Finally, conclusions and perspectives are presented in Sect. 6.

2. Pantheon+ sample

Pantheon+, as the latest sample of SNe Ia, consists of 1701 SNe Ia light curves observed from 1550 distinct SNe and covers redshift range from 0.001 to 2.26 (Brout et al. 2022; Scolnic et al. 2022). The redshift distributions of the Pantheon (Scolnic et al. 2018) and Pantheon+ samples are shown in Fig. 1. From the redshift distribution of these two samples, it is not difficult to find that there are two main differences between the new sample and the Pantheon sample. One is that the SN number has increased significantly at low redshift. There are more than 700 additional SNe in the range of $z < 0.8$, of which more than 500 SNe originated from $z < 0.08$. This is mainly because the new sample adds five large samples, including the Foundation Supernova Survey (Foundation; Foley et al. 2018), the Swift Optical/Ultraviolet Supernova Archive (SOUSA; Brown et al. 2014), the Lick Observatory Supernova Search (LOSS1; Ganeshalingam et al. 2010), the second sample from LOSS (LOSS2; Stahl et al. 2019), and the Dark Energy Survey Year 3 (DES; Brout et al. 2019; Smith et al. 2020), all of which are low-redshift surveys, except DES. The other difference is that there is a significant deletion in Pantheon+ statistics between $0.8 < z < 1.0$. The reason is that Scolnic et al. (2022) did not use SNe from the Supernova Legacy Survey (SNLS) at $z > 0.8$ considering sensitivity to the U band in model training (56 SNe in total).

Figure 2 shows the distribution (left panel) and corresponding density (right panel) of the Pantheon+ sample in the sky of the galactic coordinate system. Some previous work has pointed out that the Pantheon SNe Ia are not uniformly distributed in the sky; half of them are located in the galactic southeast. Some SNe are very concentrated, forming a belt-like structure that is the SDSS sample (Zhao et al. 2019). At the same time, Zhao et al. (2019) also investigated the effect of the inhomogeneous distribution of the Pantheon sample on the cosmic anisotropy and found that the belt-like structure plays the most important role in the Pantheon sample. In the left panel, to highlight the difference between these two samples, we mark the newly added

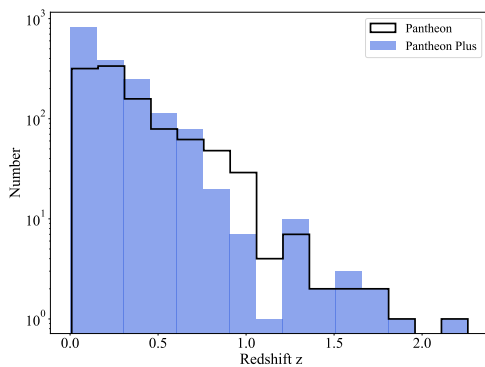


Fig. 1. Redshift distribution of the Pantheon and Pantheon+ samples.

SNe Ia in red. From the distribution of the Pantheon+ sample, we find that the distribution of the new data is still uneven across the sky. There are only fewer observations near $(l, b) \sim (300^\circ, -30^\circ)$. Its incomplete sky coverage is primarily due to the fact that the Pantheon+ sample consists of different subsamples, following multiple measurement strategies. In order to make it easier to comprehend this focus, we also plot the density distribution of the Pantheon+ sample utilizing the `plt.contour()` function¹, as shown in the right panel of Fig. 2. Color-coded values represent sample fraction per unit area. From the density distribution, we can more intuitively feel the inhomogeneity of sample distribution. As can be seen, the belt-like part of the Pantheon+ sample still plays the most important role, as in the case of the Pantheon sample, while the maximum density value changes from 0.24 to 0.21 (Hu et al. 2020). This means that the Pantheon+ sample is more uniform than the Pantheon sample. The newly added SNe Ia effectively weaken the dominance of the belt structure in the distribution. The Pantheon+ sample that is relatively uniform and rich in low redshift is very suitable for analyzing the local property of the Universe (Andrade et al. 2018; Luongo et al. 2022; Kalbouneh et al. 2023). Here, we used the RF method combined with the Pantheon+ sample to describe the all-sky distribution of cosmological parameters to study the local structure of the Universe, and the detailed analysis process is shown in the next section.

3. Region fitting method

The hemisphere comparison (HC) method proposed by Schwarz & Weinhorst (2007) has been widely used in the investigation of the cosmic anisotropy, such as the anisotropy of cosmic expansion (Deng & Wei 2018a; Zhao & Xia 2022), the acceleration scale of modified Newtonian dynamics (Zhou et al. 2017; Chang et al. 2018; Chang & Zhou 2019), and the temperature anisotropy of the CMB (Hansen et al. 2004; Bennett et al. 2013; Ghosh et al. 2016; Ferreira & Quartin 2021). The RF method we used is similar to it. Here, we provide a detailed introduction to this method. Its goal is to map the all-sky distribution of the cosmological parameters. The most important step is to generate random directions $\hat{D}(l, b)$ to pick out SNe data located in specific regions to construct subdatasets, where $l \in (0^\circ, 360^\circ)$ and $b \in (-90^\circ, 90^\circ)$ are the longitude and latitude in the galactic coordinate system, respectively. The specific region is given by condition $(\theta < \theta_{\max})$. θ is the angle between the random direction $\hat{D}(l, b)$ and the SN position. Here we refer to θ_{\max} as the screening angle used to obtain regions of different sizes, and the value

¹ https://matplotlib.org/stable/gallery/images_contours_and_fields/irregulardatagrid.html

range is $(0^\circ, 180^\circ)$. The remaining steps can be divided into three parts, which we present in the following subsections.

3.1. Fitting parameters

According to subdatasets obtained in the previous step, the corresponding best fits of the cosmological parameters are obtained by minimizing value of χ^2 ,

$$\chi^2 = \Delta\mu \mathbf{C}_{\text{stat+syst}}^{-1} \Delta\mu^T, \quad (1)$$

where $\Delta\mu$ is the difference between the observational distance modulus μ_{obs} and the theoretical distance modulus μ_{th} :

$$\Delta\mu = \mu_{\text{obs}}(z_i) - \mu_{\text{th}}(\Omega_m, H_0, z_i). \quad (2)$$

For the flat Λ CDM model, the corresponding form of μ_{th} can be written as

$$\mu_{\text{th}}(\Omega_m, H_0, z_i) = m - M = 5 \log_{10} \frac{d_L(\Omega_m, H_0, z_i)}{\text{Mpc}} + 25; \quad (3)$$

here, z_i is the peculiar-velocity-corrected CMB-frame redshift of each SN (Carr et al. 2022), m is the apparent magnitude of the source, M is the absolute magnitude, and d_L is the luminosity distance expressed in megaparsec, defined in the following equation:

$$d_L = \frac{c(1+z)}{H_0} \int_0^z \frac{dz'}{\sqrt{\Omega_m(1+z')^3 + (1-\Omega_m)}}, \quad (4)$$

where c is the speed of light.

The statistical (\mathbf{C}_{stat}) and systematic covariance matrices (\mathbf{C}_{sys}) are combined and adopted to constrain the cosmological parameters:

$$\mathbf{C}_{\text{stat+syst}} = \mathbf{C}_{\text{stat}} + \mathbf{C}_{\text{sys}}. \quad (5)$$

The datasets we used, μ_{obs} , and $\mathbf{C}_{\text{stat+syst}}$, are provided by Brout et al. (2022) and can be obtained online². $\mathbf{C}_{\text{stat+syst}}$ includes all the covariance between SNe (and also Cepheid host covariance) due to systematic uncertainties (Brout et al. 2022). \mathbf{C}_{stat} mainly includes the full distance error and measurement noise. \mathbf{C}_{sys} can manifest in three key places in the analysis: (1) from changing aspects affecting the light-curve fitting; (2) from changing redshifts that propagate to changes in distance modulus relative to a cosmological model; and (3) from changes in the simulations used for bias corrections (Brout et al. 2022). More detailed information about the covariance matrices can be found in Sect. 2.2 of Brout et al. (2022). Unlike the previous analyses (Betoule et al. 2014; Colin et al. 2019), we did not introduce an intrinsic scatter. So, in the fitting process, there are only two free parameters (Ω_m and H_0), which makes them strongly correlated. For the different subdatasets, Ω_m and H_0 are fitted simultaneously. The $\mathbf{C}_{\text{stat+syst}}$ we used were obtained by cropping the total covariance matrix according to the SNe Ia subsample. In this work, the minimization was performed employing a Bayesian Markov chain Monte Carlo (MCMC; Foreman-Mackey et al. 2013) method with the `emcee` package³. All the fittings in this paper were obtained adopting this python package. The MCMC samples were plotted utilizing the `getdist` package (Lewis 2019).

² <https://github.com/PantheonPlusSH0ES/DataRelease>

³ <https://emcee.readthedocs.io/en/stable/>

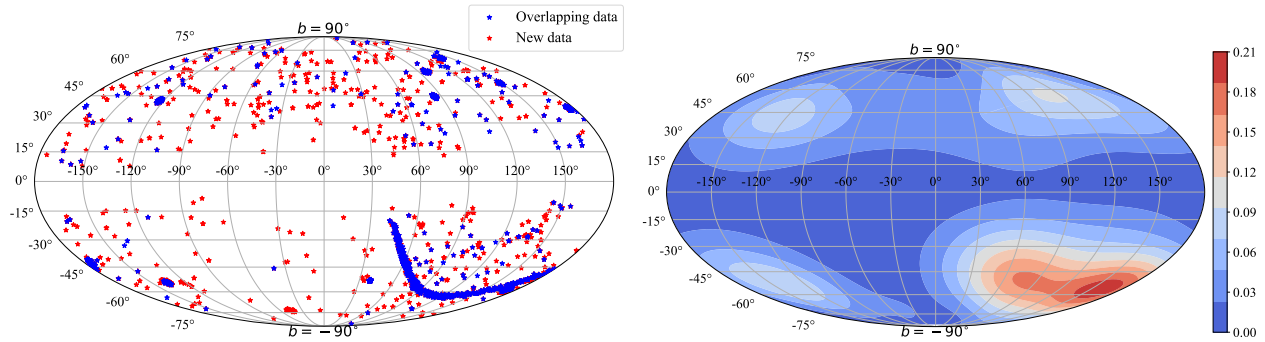


Fig. 2. Distribution and corresponding density contour in the galactic coordinate system. Left panel shows the SNe distribution of the Pantheon sample. Red and blue points represent the new added SNe and the SNe where the Pantheon sample and the Pan sample overlap, respectively. Right panel shows the corresponding density contour.

3.2. All-sky distribution

During the calculation, we repeated 5000 random directions $\hat{D}(l, b)$, that is, 5000 sets of best fitting results (Ω_m and H_0). Based on the fitting results, the all-sky distributions of Ω_m and H_0 are mapped, respectively. From the distribution of Ω_m and H_0 , we can obtain information concerning the local matter underdensity and cosmic anisotropy, respectively. In order to describe the degree of deviation from the cosmological principle, we define a parameter $D_{\max}(\sigma)$ whose form is as follows:

$$D_{\max}(\sigma) = \frac{P_{\max} - P_{\min}}{\sqrt{\sigma_{P_{\max}}^2 + \sigma_{P_{\min}}^2}}. \quad (6)$$

Here, P_{\min} and P_{\max} are the minimum value and the maximum value of the best fitting results, respectively. $\sigma_{P_{\min}}$ and $\sigma_{P_{\max}}$ are the corresponding 1σ error. The local matter underdensity direction and the preferred direction of cosmic anisotropy are marked by the corresponding location of the lowest Ω_m and the largest H_0 . The corresponding 1σ regions are plotted in terms of the values of P_0 , which is calculated from

$$1.00(\sigma) \geq \frac{P_0 - P_{\text{fit}}}{\sqrt{\sigma_{P_0}^2 + \sigma_{P_{\text{fit}}}^2}}, \quad (7)$$

where P_{fit} , representing the lowest Ω_m constraint or the largest H_0 constraint, is used to find the 1σ range of the local matter underdensity direction or the preferred direction. $\sigma_{P_{\text{fit}}}$ represents the corresponding error. P_0 represents the constraints that are consistent with P_{fit} within 1σ error, and σ_{P_0} are the corresponding 1σ values. We note that P_0 and σ_{P_0} are filtered from the total Ω_m/H_0 fitting results depending on Eq. 7. Here, P_0 and P_{fit} are completely independent and were obtained using different SNe subsamples.

3.3. Statistical analyses

In order to examine whether the discrepancy degree of the cosmological parameters from the Pantheon+ sample is consistent with statistical isotropy, we plan to carry out statistical isotropic analyses. To achieve this, we spread the original data set evenly across the sky. After that, we were able to obtain the D_{\max} for the isotropic dataset. Meanwhile, an additional isotropic analysis was also considered. We preserved the spatial inhomogeneity of real sample and then randomly distributed the real dataset, which randomly redistributed the distance moduli and redshift combination to real-data positions (RP) only. Given the limitations of

computing time, we repeated it 500 times; this gave acceptable statistics. For convenience, we refer to these two approaches as isotropy analysis and isotropy RP analysis.

4. Results

We first give the best fitting results in the flat Λ CDM model employing the full Pantheon+ sample, $\Omega_m = 0.36 \pm 0.02$, and $H_0 = 72.83 \pm 0.23 \text{ km s}^{-1} \text{ Mpc}^{-1}$. The results are in line with the previous research (Brout et al. 2022), except that the 1σ error of H_0 is reduced. The main reason is that we utilized the standardized distance modulus (μ_{obs} ; Tripp 1998), where fiducial M has been determined from SH0ES 2021 Cepheid host distances (Riess et al. 2022).

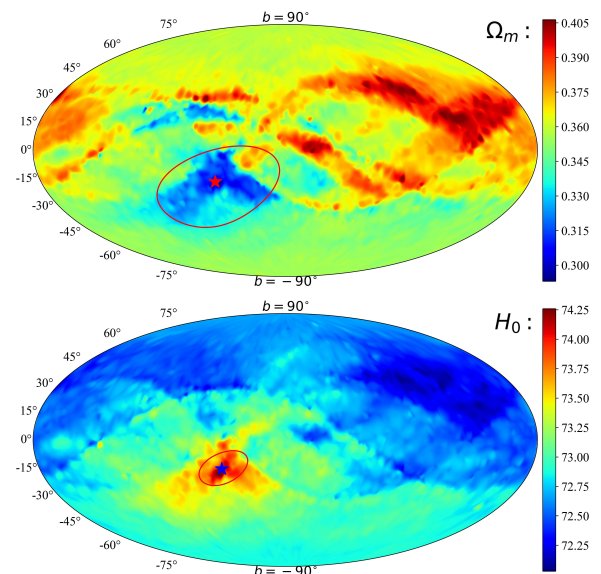


Fig. 3. All-sky distribution of cosmological parameters utilizing the Pantheon+ sample combined with the 90° RF method. The upper and the lower panels show the results of Ω_m and H_0 , respectively. The corresponding values of $D_{\max}(\sigma)$ are 3.29σ and 4.48σ , respectively. The star marks the directions of the lowest Ω_m (upper panel) and the largest H_0 (lower panel), and the red circle outlines the corresponding 1σ areas. The directions and 1σ areas are parameterized as $\Omega_{m,\min}(308.4^{+47.6}_{-48.7}, -18.2^{+21.1}_{-28.8})$ and $H_{0,\max}(313.4^{+19.6}_{-18.2}, -16.8^{+11.1}_{-10.7})$.

After that, using the RF method with a screening angle $\theta_{\max} = 90^\circ$, we mapped the all-sky distribution of Ω_m and H_0 and draw the 1σ regions of local matter underdensity and cos-

mic anisotropy, as shown in the upper panel and lower panel of Fig. 3, respectively. In Fig. 3, the range of Ω_m and H_0 are (0.29, 0.41) and (72.03, 74.26), respectively. The corresponding differences are $\Delta\Omega_m = 0.12$ and $\Delta H_0 = 2.23 \text{ km s}^{-1} \text{ Mpc}^{-1}$. The values of D_{max} to Ω_m and H_0 are $D_{\text{max},\Omega_m} = 3.29\sigma$ and $D_{\text{max},H_0} = 4.48\sigma$, respectively. In the upper panel of Fig. 3, the minimum constraint of Ω_m is $\Omega_{m,\text{min}} = 0.29^{+0.03}_{-0.02}$ (1σ) and the corresponding constraint for H_0 is $74.11^{+0.40}_{-0.40} \text{ km s}^{-1} \text{ Mpc}^{-1}$. The direction and corresponding 1σ range that can be adopted to describe the local matter underdensity are

$$(l, b) = (308.4^{+47.6}_{-48.7}, -18.2^{+21.1}_{-28.8}). \quad (8)$$

The lower panel of Fig. 3 shows the corresponding all-sky distribution of the Hubble expansion. The maximum constraint of H_0 is $H_{0,\text{max}} = 74.26 \pm 0.39 \text{ km s}^{-1} \text{ Mpc}^{-1}$, and the corresponding constraint of Ω_m is $0.30^{+0.03}_{-0.03}$. Its confidence contours are shown in Fig. 4, marked with blue lines. The preferred direction of cosmic anisotropy and corresponding 1σ range are

$$(l, b) = (313.4^{+19.6}_{-18.2}, -16.8^{+11.1}_{-10.7}). \quad (9)$$

In Fig. 4, we also give the best fitting results of opposite directions; that is, $H_{0,\text{min}} = 72.14^{+0.27}_{-0.27} \text{ km s}^{-1} \text{ Mpc}^{-1}$ and $\Omega_m = 0.40^{+0.02}_{-0.02}$, which are marked with red lines.

The statistical isotropic results shown in Fig. 5 can be well described by Gaussian functions. For the isotropy analysis, the statistical significances (α) of the real data are 2.78σ for Ω_m anisotropy (upper, purple panel) and 3.96σ for H_0 anisotropy (upper, blue panel). The statistical significance (β) of the real data given by the isotropy RP analysis are 2.34σ for Ω_m anisotropy (lower, purple panel) and 3.15σ for H_0 anisotropy (lower, blue panel).

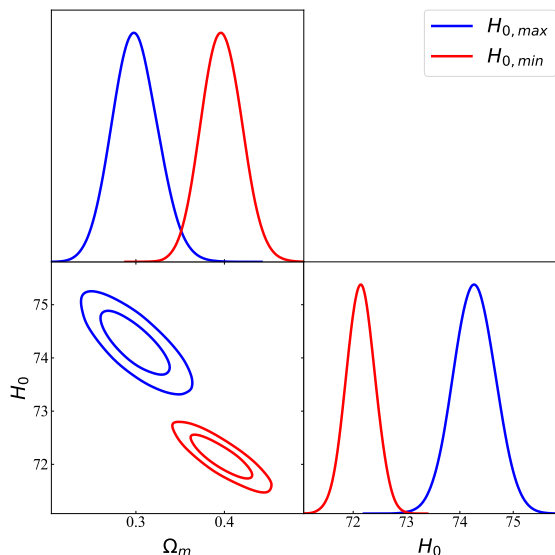


Fig. 4. Confidence contours (1σ and 2σ) and marginalized likelihood distributions for the parameter space (Ω_m and H_0) in the spatially flat Λ CDM model from the SNe Ia subsamples, which corresponds to $H_{0,\text{min}}$ (red line) and $H_{0,\text{max}}$ (blue line). The best fitting results of preferred direction are $H_{0,\text{max}} = 74.26^{+0.40}_{-0.39} \text{ km s}^{-1} \text{ Mpc}^{-1}$, $\Omega_m = 0.30^{+0.03}_{-0.03}$ (blue line). The best fitting results of opposite directions are $H_{0,\text{min}} = 72.14^{+0.27}_{-0.27} \text{ km s}^{-1} \text{ Mpc}^{-1}$ and $\Omega_m = 0.40^{+0.02}_{-0.02}$ (red line).

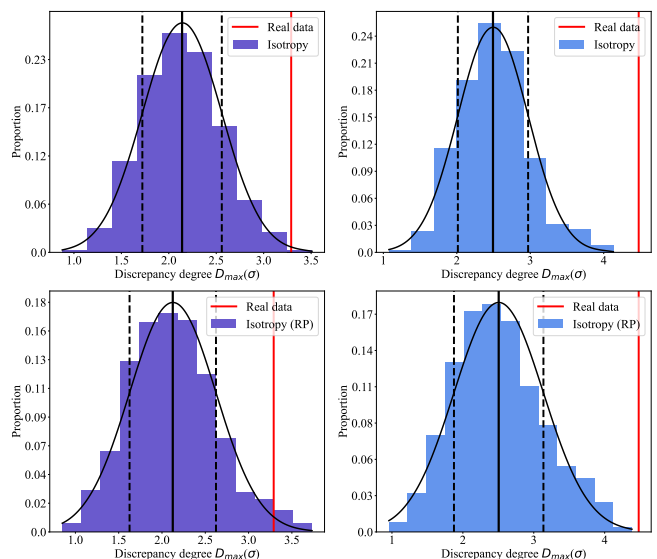


Fig. 5. Distribution of discrepancy degree D_{max} in 500 simulated isotropic datasets. The upper two panels show the results of statistical isotropic analyses (isotropy). The lower two panels show the results of statistical isotropic analyses that preserve the spatial inhomogeneity of real data (isotropy RP). Purple and blue represent the statistical results of Ω_m and H_0 . The black curve is the best fit to the Gaussian function. The solid black and vertical dashed lines are commensurate with the mean and the standard deviation, respectively. The red lines represent the discrepancy degree from the real data. For the isotropy analyses, the statistical significance of the real data are 2.78σ for Ω_m anisotropy and 3.96σ for H_0 anisotropy. For the isotropy RP analyses, the statistical significance of the real data are 2.34σ and 3.15σ for Ω_m and H_0 anisotropy, respectively.

4.1. Reanalyses at low redshift

Recently, Hu & Wang (2022b) reported a late-time transition of H_0 ; that is, H_0 changes from a low value to a high one from early to late cosmic time by combining the GP method and $H(z)$ data. The H_0 transition occurs at $z \sim 0.49$. From other observations, a similar descending behavior of H_0 has been found adopting other methods (see Hu & Wang (2023) for a review of H_0 descending trend). Around $z \sim 0.40$, H_0 starts to decrease (Jia et al. 2023). Both the transition behavior and the descending trend of H_0 can effectively alleviate the Hubble tension. Kelly et al. (2023) gave new H_0 measurements from the gravitationally lensed SNe Ia Refsdal (Refsdal 1964). The redshifts of the lens and the source are 0.54 and 1.49 (Kelly et al. 2015), respectively. Utilizing eight cluster lens models, they inferred $H_0 = 64.80^{+4.40}_{-4.30} \text{ km s}^{-1} \text{ Mpc}^{-1}$. Then, using the two models most consistent with observations, they found $H_0 = 66.60^{+4.10}_{-3.30} \text{ km s}^{-1} \text{ Mpc}^{-1}$. Marking the values of lensing redshift and H_0 on Fig. 3 in Hu & Wang (2022b) and Fig. 4 in Jia et al. (2023), we find that these results are in good agreement with the evolutionary behaviors of H_0 . Motivated by the H_0 special behaviors in the late-time universe, we plan to construct a low-redshift subsample based on the Pantheon+ sample to make a reanalyses. According to the previous research (Hu & Wang 2022b; Jia et al. 2023), and considering the need for a sufficient sample size, we decided to select 1218 SNe with redshift less than 0.30 in the Pantheon+ sample to construct sub-sample (named the lp+ sample). Detailed steps and results are as follows.

At first, we give the cosmological constraint in the flat Λ CDM model using the lp+ sample; that is, $\Omega_m = 0.44 \pm 0.04$ and $H_0 = 72.43 \pm 0.30 \text{ km s}^{-1} \text{ Mpc}^{-1}$, which is consistent with the re-

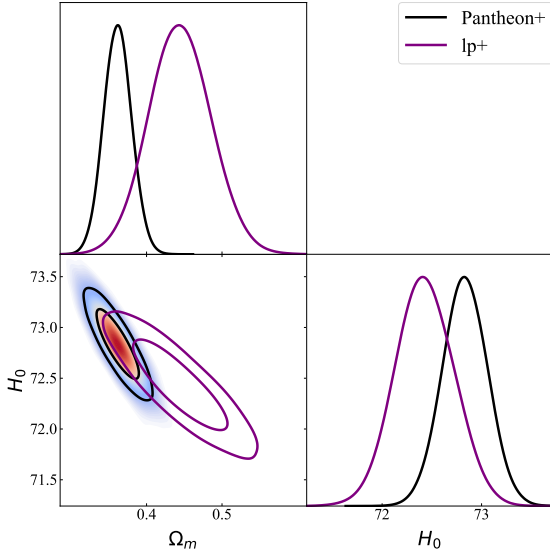


Fig. 6. Confidence contours (1σ and 2σ) and marginalized likelihood distributions for parameters space (Ω_m and H_0) in the spatially flat Λ CDM model from the Pantheon+ sample and the lp+ sample. For the former, the best fits are $\Omega_m = 0.36 \pm 0.02$ and $H_0 = 72.83 \pm 0.23$ km s $^{-1}$ Mpc $^{-1}$ (black line). For the latter, the best fits are $\Omega_m = 0.44 \pm 0.04$ and $H_0 = 72.43 \pm 0.30$ km s $^{-1}$ Mpc $^{-1}$ (purple line).

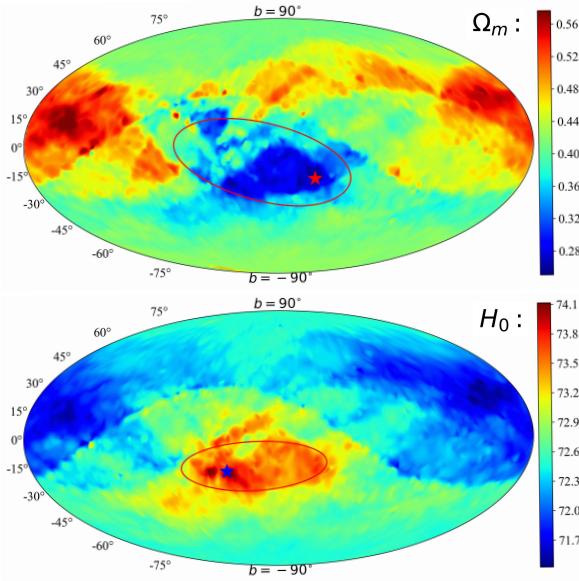


Fig. 7. All-sky distribution of cosmological parameters utilizing the $z < 0.30$ part of Pantheon+ sample (lp+ sample) combined with the 90° RF method. The upper and the lower panel show the results of Ω_m and H_0 , respectively. The corresponding values of $D_{\max}(\sigma)$ are 4.17σ and 4.49σ , respectively. The star marks the directions of the lowest Ω_m (upper panel) and the largest H_0 (lower panel), and the red circle outlines the corresponding 1σ areas. The directions and 1σ areas are parameterized as $\Omega_m (26.4^{+26.3}_{-100.9}, -19.3^{+35.4}_{-17.0})$, $H_0 (321.9^{+72.5}_{-33.5}, -18.9^{+16.6}_{-11.5})$.

results from the full Pantheon+ sample and from Fig. 16 in Brout et al. (2022). For ease of comparison, we give the constraint results of the Pantheon+ and lp+ samples in Fig. 6. Then, we reproduced the previous analyses. The all-sky distribution, the cosmological constraints, and the isotropic statistic results are shown in Figs. 7, 8, and 9, respectively. From Fig. 7, it is easy to obtain the ranges of constraints: $\Omega_m (0.25, 0.58)$ and $H_0 (71.43, 74.11)$ km s $^{-1}$ Mpc $^{-1}$. The corresponding differences are $\Delta\Omega_m =$

0.33 and $\Delta H_0 = 2.68$ km s $^{-1}$ Mpc $^{-1}$. By calculation, we obtain $D_{\max, \Omega_m} = 4.17\sigma$ and $D_{\max, H_0} = 4.49\sigma$. The directions and 1σ regions of the local matter underdensity and cosmic anisotropy given by the reanalyses using the lp+ sample are

$$(l, b) = (26.4^{+26.3}_{-100.9}, -19.3^{+35.4}_{-17.0}) \quad (10)$$

and

$$(l, b) = (321.9^{+72.5}_{-33.5}, -18.9^{+16.6}_{-11.5}). \quad (11)$$

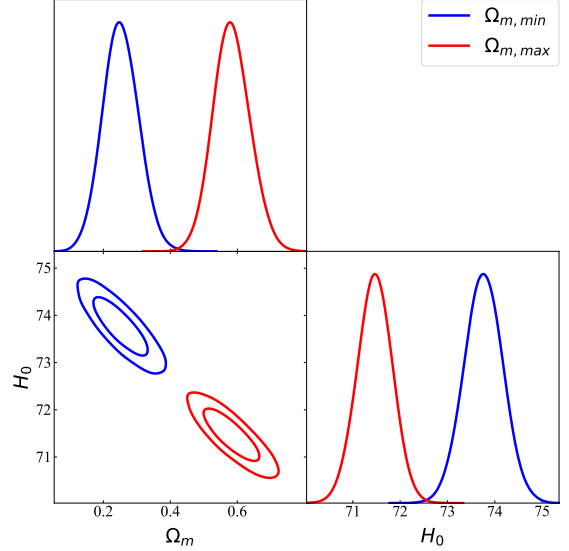


Fig. 8. Confidence contours (1σ and 2σ) and marginalized likelihood distributions for the parameters space (Ω_m and H_0) in the spatially flat Λ CDM model from the SNe Ia subsamples, which corresponds to $\Omega_{m, \min}$ (blue line) and $\Omega_{m, \max}$ (red line). The best fitting results of preferred direction are $\Omega_{m, \min} = 0.25^{+0.05}_{-0.05}$ and $H_0 = 73.76^{+0.41}_{-0.41}$ km s $^{-1}$ Mpc $^{-1}$ (blue line). The best fitting results of opposite direction are $\Omega_{m, \max} = 0.58^{+0.06}_{-0.05}$ and $H_0 = 71.46^{+0.37}_{-0.37}$ km s $^{-1}$ Mpc $^{-1}$ (red line).

The constraints corresponding to preferred directions of the local matter underdensity and cosmic anisotropy are $\Omega_{m, \min} = 0.25 \pm 0.05$ and $H_0 = 73.76 \pm 0.41$ km s $^{-1}$ Mpc $^{-1}$, and $H_{0, \max} = 74.11^{+0.47}_{-0.48}$ km s $^{-1}$ Mpc $^{-1}$ and $\Omega_m = 0.27 \pm 0.06$. In Fig. 8, we show the confidence contours in the preferred and opposite directions of the local matter underdensity. The isotropic statistical results from the lp+ sample are shown in Fig. 9. For the isotropy analysis, the statistical significance of the real data are 3.68σ for Ω_m anisotropy (upper, purple panel) and 3.01σ for H_0 anisotropy (upper, blue panel). The isotropy RP analysis gives the statistical significance of the real data, which is 2.09σ for Ω_m anisotropy (lower, purple panel) and 1.35σ for H_0 anisotropy (lower, blue panel).

4.2. Different screening angles θ_{\max}

Theoretically, if there are enough SNe data distributed at different redshifts in a certain direction, the constraints of the cosmological parameters in this direction can be obtained (Lin et al. 2016a; Deng & Wei 2018b; Kumar Aluri et al. 2023). Due to the limitation of the number of observational data, it is currently impossible to directly give the result of the limitation of cosmological parameters in a certain direction. Therefore, the 90° RF method is usually used to derive the cosmological constraint of the single direction, that is the HC method (Schwarz & Weinhorst 2007). In this subsection, we try to find out the limit value

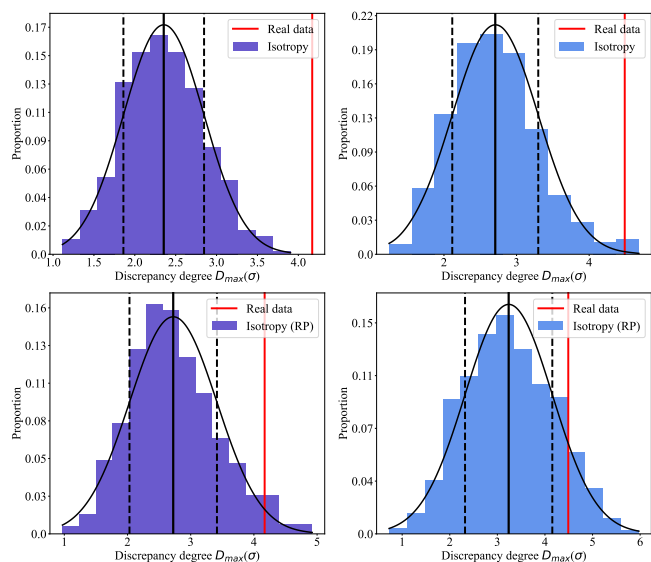


Fig. 9. Distribution of discrepancy degree D_{\max} in 500 simulated isotropic datasets. The upper two panels show the results of statistical isotropic analyses (isotropy). The lower two panels show the results of statistical isotropic analyses that preserve the spatial inhomogeneity of real data (isotropy RP). The purple and blue represent the statistical results of Ω_m and H_0 . The black curve is the best fit to the Gaussian function. The solid black and vertical dashed lines are commensurate with the mean and the standard deviation, respectively. The red lines represent the discrepancy degree from the real data. For the isotropy analyses, the statistical significance of the real data are 3.68σ for Ω_m anisotropy and 3.01σ for H_0 anisotropy. For the isotropy RP analyses, the statistical significance of the real data are 2.09σ and 1.35σ for Ω_m and H_0 anisotropy, respectively.

of θ_{\max} that is suitable for the Pantheon+ sample by mapping the all-sky distributions of the cosmological parameters Ω_m and H_0 with different θ_{\max} . Considering the limitations of computing time, only three angles (30° , 45° and 60°) are chosen. Take $\hat{D}(60^\circ, 0^\circ)$ as an example, Figure 10 shows the schematic diagram of the RF method with different θ_{\max} . Smaller θ_{\max} will reduce the overlapping data between sub-samples generated by adjacent random directions. The corresponding all-sky distributions will present more details on the current state of the Universe. For the Pantheon+ sample, lowering θ_{\max} can be expected to produce some poorly fitting results. Therefore, we give a constrained culling of possibly poor constraints. Here, we set a loose condition of $0 < \Omega_m < 1.00$. The final results are shown in Fig. A.1. For the screening angles 30° , 45° , and 60° , the proportions of the wrong fitting results are 30.34%, 6.47%, and 0.70%, respectively. From Fig. A.1, we find that $\theta_{\max} = 60^\circ$ seems to be the limit that the Pantheon+ sample can bear. At this time, nearly 100% (99.30%) of the random directions (\hat{D}) can be reliably constrained.

In Fig. A.2, we give the best fits for the hemispheres where $\Omega_{m,\min}$ and $\Omega_{m,\max}$ are located. We find that taking into account narrowing the screening angle θ_{\max} significantly increases the 1σ error of Ω_m constraints. The reduced chi-square (χ_r^2) corresponding to $\Omega_{m,\min}$ is 0.69, which is much smaller than 1.00. Therefore, we only show the analysis results of H_0 . The all-sky distribution, cosmological constraints and isotropic statistical results are displayed in Figs. 11, 12, and 13, respectively. As shown in Fig. 11, the preferred direction of cosmic anisotropy given by the H_0 distribution is $(351.4^{+28.0}_{-64.2}, -8.8^{+40.3}_{-27.8})$, and D_{\max} is 4.39σ . The corresponding constraints of a preferred direction are

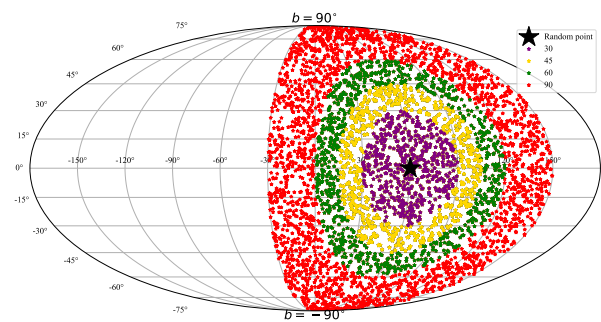


Fig. 10. Schematic diagram of the RF method with different screening angles including 30° , 45° , 60° , and 90° . Black star represents the random direction $\hat{D}(60^\circ, 0^\circ)$.

$H_{0,\max} = 74.81^{+0.71}_{-0.71}$ km s $^{-1}$ Mpc $^{-1}$ and $\Omega_m = 0.28^{+0.05}_{-0.04}$. The statistical isotropy results show that the statistical confidences of the real data are 1.70σ for the isotropy analysis and 2.27σ for the isotropy RP analysis.

All results in this section are summarized in Table 1. Additionally, we provide the reduced chi-square χ_r^2 for the anisotropic direction.

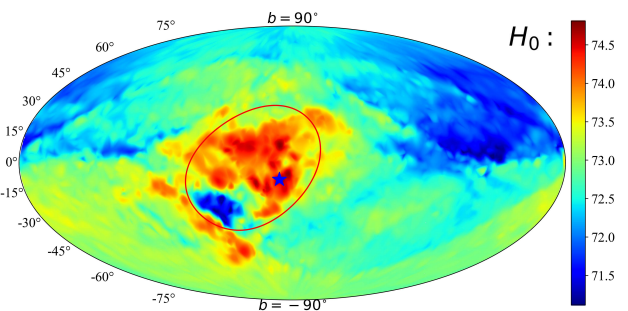


Fig. 11. All-sky distribution of H_0 utilizing Pantheon+ sample combined with 60° RF method. The direction and 1σ area are parameterized as $(351.4^{+28.0}_{-64.2}, -8.8^{+40.3}_{-27.8})$. The statistical discrepancy D_{\max} is 4.39σ .

5. Discussion

All-sky distributions of cosmological parameters (Ω_m and H_0) from the total sample show that there is an obvious local underdensity area and a preferred direction of cosmic expansion. From Fig. 3, we can find that there are some weird features that may result from fluctuations in the matter density, or fluctuations in the Hubble expansion (Gurzadyan, V. G. et al. 2023). In the upper panel, the red and blue areas represent areas of higher and lower material density, respectively. In the lower panel, the red areas represent regions of higher Hubble expansion. The continuity of these structures suggests that the results may not be sensitive to individual SNe Ia. Combining these two panels of Fig. 3, we find that the local underdensity in the upper panel overlaps with the higher Hubble expansion (cosmic anisotropy) in the lower panel. This may imply that local matter density might be responsible for the anisotropy of the accelerated expansion of the Universe. The corresponding 1σ regions are quite obvious. In other words, the 1σ range of Ω_m is significantly larger than that of H_0 . The main reason for this phenomenon might be that these two parameters have different sensitivities on the redshift. The inhomogeneous matter-density distribution could also affect the deceleration parameter q_0 , causing a larger q_0 in the local underdensity. Theoretically, the maximum q_0 direction

Table 1. Detailed information of analysis results from the all-sky distribution of cosmological parameters.

Sample	θ_{\max}^a	$\Omega_{m,min}$	H_0 ($\text{km s}^{-1} \text{Mpc}^{-1}$)	D_{\max}^b (σ)	α^c (σ)	β^d (σ)	Direction (l, b)	χ_r^2
Pantheon+	90°	$0.29^{+0.03}_{-0.02}$	$74.11^{+0.40}_{-0.40}$	3.29	2.78	2.34	$(308.4^{+47.6}_{-48.7}, -18.2^{+21.1}_{-28.8})$	0.94
Pantheon+	60°	$0.23^{+0.20}_{-0.17}$	$74.05^{+1.00}_{-1.00}$	-	-	-	-	0.69*
lp+	90°	$0.25^{+0.05}_{-0.05}$	$73.76^{+0.41}_{-0.41}$	4.17	3.68	2.09	$(26.4^{+26.3}_{-100.9}, -19.3^{+35.4}_{-17.0})$	0.94
Sample	θ_{\max}^a	$H_{0,max}$ ($\text{km s}^{-1} \text{Mpc}^{-1}$)	Ω_m	D_{\max}^b (σ)	α^c (σ)	β^d (σ)	Direction (l, b)	χ_r^2
Pantheon+	90°	$74.26^{+0.40}_{-0.39}$	$0.30^{+0.03}_{-0.03}$	4.48	3.96	3.15	$(313.4^{+19.6}_{-18.2}, -16.8^{+11.1}_{-10.7})$	0.98
Pantheon+	60°	$74.81^{+0.71}_{-0.71}$	$0.28^{+0.05}_{-0.04}$	4.39	1.70	2.27	$(351.4^{+28.0}_{-64.2}, -8.8^{+40.3}_{-27.8})$	0.99
lp+	90°	$74.11^{+0.47}_{-0.48}$	$0.27^{+0.06}_{-0.06}$	4.49	3.01	1.35	$(321.9^{+72.5}_{-33.5}, -18.9^{+16.6}_{-11.5})$	1.14

^a θ_{\max} is the screening angle.

^b D_{\max} represents the degree of deviation from the cosmological principle; the larger the value, the higher the degree of deviation.

^c α indicates the statistical significance of real data from the isotropy analysis.

^d β indicates the statistical significance of real data from the isotropy RP analysis.

* For the RF (60°) results of the Pantheon+ sample, the reduced chi-square (χ_r^2) corresponding to $\Omega_{m,min}$ is 0.69, which is much smaller than 1.00. Therefore, the RF (60°) results are not given.

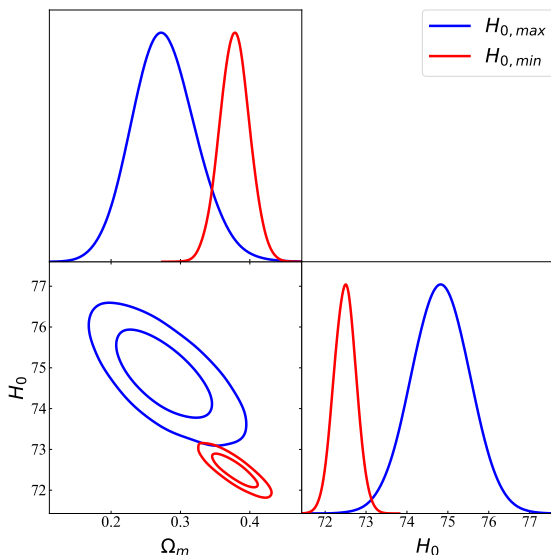


Fig. 12. Confidence contours (1σ and 2σ) and marginalized likelihood distributions for parameter space (Ω_m and H_0) in the spatially flat Λ CDM model from the SNe Ia subsamples, which corresponds to $H_{0,min}$ (red line) and $H_{0,max}$ (blue line). The best fitting results of preferred direction are $H_{0,max} = 74.81^{+0.71}_{-0.71} \text{ km s}^{-1} \text{Mpc}^{-1}$ and $\Omega_m = 0.28^{+0.05}_{-0.04}$ (blue line). The best fitting results of opposite directions are $H_{0,min} = 72.49^{+0.27}_{-0.27} \text{ km s}^{-1} \text{Mpc}^{-1}$ and $\Omega_m = 0.38^{+0.02}_{-0.02}$ (red line).

should be consistent with the local underdensity direction. For the determination of H_0 value with local distance indicators, the observed H_0 values depend on the average matter density within the distance range covered (Böhringer et al. 2020). Combining the Ω_m distribution, we can find that there might be a region of low matter density, which leads to a smaller average matter density which makes the H_0 measurements higher. Therefore, the local underdensity can exacerbate the magnitude of the Hubble Tension (Böhringer et al. 2020; Hu & Wang 2022b; Jia et al. 2023; Hu & Wang 2023). In other words, accounting for the local underdensity or cosmic isotropy could alleviate the current Hubble tension.

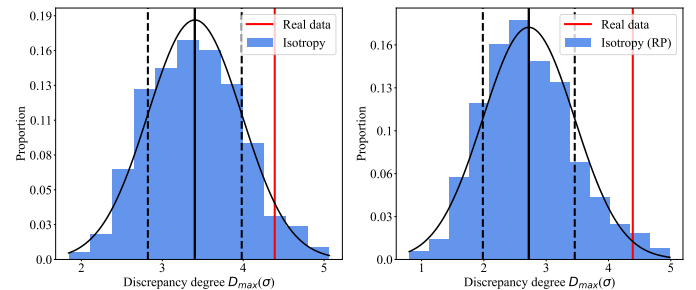


Fig. 13. Distribution of discrepancy degree D_{\max} obtained from H_0 distribution in 500 simulated isotropic datasets. The left panel and right panel show the results of isotropy and isotropy RP analyses, respectively. The black curve is the best fit to the Gaussian function. The solid black and vertical dashed lines are commensurate with the mean and the standard deviation, respectively. The red lines represent the discrepancy degree from the real data. The statistical significances of the real data are 1.70σ for the isotropy analysis and 2.27σ for the isotropy RP analysis.

From Fig. 5, we find that the isotropy analysis shows an obvious statistical significance, especially the study of H_0 , which is nearly 4σ . Afterwards, considering the spatial inhomogeneity of the real sample, we performed the isotropy RP analysis and find a slight decrease in statistical significance. This suggests that inhomogeneous spatial distribution of a real sample can increase the deviation from isotropy. In addition, combining all the statistical results, we find the statistical significances of H_0 anisotropy are more obvious than that of Ω_m anisotropy. From the distributions of a single parameter, we find an obvious anisotropy. But the effect of one on the other might be canceled out, making the all-sky distribution of luminosity distances isotropic. Therefore, in order to clear up this doubt, we plotted the all-sky distribution of luminosity distances when z is set to 2.26 and give the relationships between d_L and z of two anisotropic hemispheres, as shown in Figs. 14 and 15, respectively. The results of these two figures show that the all-sky distribution of luminosity distances is also anisotropic and the $d_L - z$ relationships obtained from two anisotropic hemispheres have obvious differences. The direction of larger luminosity distance is consistent with the anisotropy direction from the Pantheon+ sample. All in all, our investiga-

tions from the Pantheon+ sample display an inhomogeneous and anisotropic universe, and the statistical results show no low confidence level.

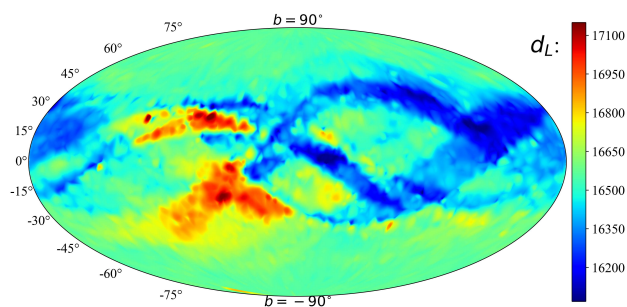


Fig. 14. All-sky distribution of luminosity distance d_L utilizing the Pantheon+ sample combined with the 90° RF method. Here, we fix $z = 2.26$.

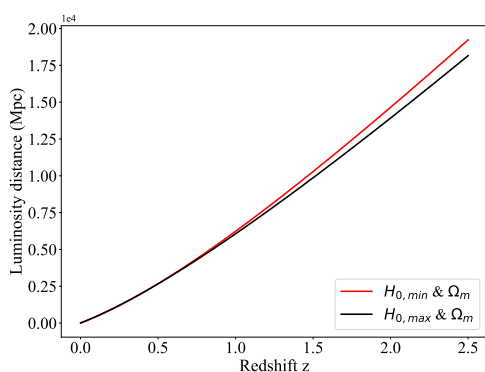


Fig. 15. Relationships between d_L and z of two anisotropic hemispheres using the two sets of best fits ($H_{0,min}$, Ω_m and $H_{0,max}$, Ω_m) in the H_0 distribution.

Motivated by recent research (Krishnan et al. 2020, 2021b; Dainotti et al. 2021, 2022a; Colgáin et al. 2022; Hu & Wang 2022b; Ó Colgáin et al. 2022; Jia et al. 2023; Malekjani et al. 2023) hinting that $H_{0,z}$ might evolve with redshift, we conducted reanalyses using the low-redshift (lp+) sample. If $H_{0,z}$ evolves with redshift (may be caused by the local void, and so on), then the measured H_0 of low-redshift and high-redshift SNe samples are different. In that case, if the redshift distribution is not uniform across the sky, this could create biases in the anisotropy detection, especially when the full sample is used; moreover, the redshift range is wider. The value of H_0 obtained from the higher redshift hemisphere is smaller than that obtained from the lower redshift hemisphere. Severely uneven redshift distribution might lead to an increase in the degree of anisotropy or a bias in the anisotropy detection. The reanalysis results are similar to those of the Pantheon+ sample and verify our previous findings. From the results of the lp+ sample (Fig. 7), we find that directions of the local matter underdensity and cosmic anisotropy given by the lp+ sample are inconsistent. Comparing the results in Figs. 4 and 8, we can find that the best fits of the two anisotropic hemispheres obtained from the lp+ sample are significantly worse than the results of the total sample. In Fig. 16, we also show the relationship between D_{max} and z_{max} , the detailed information are display in Table 2. From Fig. 16, we can find that D_{max} changes with z_{max} , and has a maximum value near $z_{max} = 0.30$. This might imply that the structure of the Universe changes with redshift. In addition, we also find that the influence of redshift on the all-

Table 2. Detailed information on the investigation of the relationship between the discrepancy degree D_{max} and z_{max} .

z_{max}	Number	$D_{max}(\Omega_m)$ (σ)	$D_{max}(H_0)$ (σ)
0.10	747	2.31	3.14
0.20	962	3.03	3.76
0.30	1218	4.17	4.49
0.40	1399	3.43	4.11
0.50	1497	2.81	3.80
0.60	1575	2.60	3.74
1.00	1677	3.07	4.11
2.26	1701	3.29	4.48

* D_{max} represents the degree of deviation from the cosmological principle, and the larger the value, the higher the degree of deviation.

sky distribution of Ω_m is larger than that of H_0 . Finally, from the statistical results of lp+ sample, we also find that the statistical significance obtained from the isotropy RP analysis are lower than that from the isotropy analysis. This finding confirms that inhomogeneous spatial distribution of a real sample can increase the deviation from isotropy.

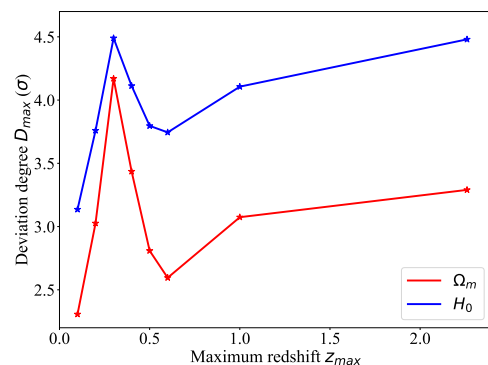


Fig. 16. Relationship between discrepancy degree D_{max} and z_{max} .

Theoretically, the screening angle θ_{max} in the RF method can be any value between 0° and 180° . However, due to the limitations of real data in quantity, spatial part, and redshift distribution, θ_{max} cannot be selected arbitrarily. In Sect. 4.2, we combine the RF method with the latest Pantheon+ sample, hoping to find a suitable screening angle θ_{max} . The analysis results are shown in Fig. A.1. Finally, we find that the screening angle θ_{max} of the Pantheon+ sample is 60° . Then, based on the 60° RF method, we restudied the Pantheon+ sample. The corresponding results are shown in Figs. 11, 12, and 13. From Fig. 11, we find that there is a small area (314.16° , -22.92°) with a lower H_0 value in the higher H_0 area, but this structure does not appear in the RF (90°) results. The lower H_0 area may be caused by high material density structures (e.g. dark matter halo) or statistical uncertainty. Narrowing the screening angle reduces the number of SNe constraining cosmological parameters, which may increase the uncertainty of the constraint. We performed a bootstrap resampling of the sample (ignoring the direction, repeated 2000 times) to study the dependence of the best-fit result error and D_{max} on the number of SNe Ia used. Here, the number of SNe ranges from 100 to 700, with a total of seven groups. From the results of Fig. 17, we can find that the average error and D_{max} increases as the used number of SNe decreases. The number of SNe used signif-

icantly affects the average error but does not significantly affect the D_{\max} value. The D_{\max} difference caused by the reduction in number is much smaller than the total D_{\max} . The preferred direction of cosmic anisotropy using the RF method with $\theta_{\max} = 60^\circ$ is in line with that using $\theta_{\max} = 90^\circ$ within a 1σ error. However, narrowing the screening angle means that the statistical significance of the isotropy analyses are significantly reduced. Interestingly, unlike previous findings, the statistical significance of the isotropy RP analysis is actually higher than that of the isotropy one.

Overall, we find that the all-sky distributions of cosmological parameters deviate significantly from isotropy, as shown in Figs. 3, 7, and 11. All preferred directions we obtained are consistent with each other within a 1σ range, and they are in line with previous research that traced the anisotropy of Ω_m and H_0 (Antoniou & Perivolaropoulos 2010; Cai & Tuo 2012; Kalus et al. 2013; Chang & Lin 2015; Hu et al. 2020) and other dipole researches (Wang & Wang 2014; Yang et al. 2014; Lin et al. 2016b; Pandey 2017; Chang & Zhou 2019; Dam et al. 2023). However, they are different from those of Luongo et al. (2022) and McConville & Colgáin (2023), which are consistent with the results of the CMB dipole (Planck Collaboration et al. 2016, 2020a). In addition, comparing with other independent observations (as shown in Table 3) including the CMB dipole (Planck Collaboration et al. 2016, 2020a), dark flow (Abdalla et al. 2022), bulk flow (Turnbull et al. 2012; Feix et al. 2017; Watkins et al. 2023), and galaxy cluster (Migkas et al. 2021), it is easy to find that the directions of the larger H_0 and the smaller Ω_m are not consistent with the CMB dipole (Planck Collaboration et al. 2016, 2020a), but they coincide with the bulk flow (Turnbull et al. 2012; Feix et al. 2017; Watkins et al. 2023) and the galaxy cluster (Migkas et al. 2021). To facilitate understanding, we aggregated these results with the ones we obtained, marking them on the galactic coordinate system, as shown in Fig. 18. The effect of peculiar velocities and the bulk flow on SNe Ia cosmology has already been discussed (Hui & Greene 2006; Davis et al. 2011; Betoule et al. 2014; Rameez et al. 2018). They can make a tiny shift in the best-fit cosmological parameters and the preferred direction locally (Colin et al. 2019).

6. Conclusions and perspectives

In this paper, we propose the RF method for the first time and combine this method with the Pantheon+ sample to test the cosmological principle. From the matter density and the Hubble expansion distributions mapped using the RF method, we find that the all-sky distributions of cosmological parameters deviate significantly from isotropy. The corresponding distribution of luminosity distance also deviates from isotropy; that is, the d_L - z relation actually diverges from region to region. Results of statistical isotropy analyses (isotropy and isotropy RP) show relatively high confidence levels: 2.78σ (isotropy) and 2.34σ (isotropy RP) for the local matter underdensity, 3.96σ (isotropy) and 3.15σ (isotropy RP) for the cosmic anisotropy. Comparing the results of statistical isotropy analyses, we find that inhomogeneous spatial distribution of real sample can increase the deviation from isotropy. The statistical significations of H_0 anisotropy are more obvious than that of Ω_m anisotropy. This might hint that parameter H_0 is more sensitive to cosmic anisotropy. The similar results and findings are found from reanalyses of the lp+ sample and the lower screening angle ($\theta_{\max} = 60^\circ$), but with a slight decrease in statistical significance. In addition, we find that D_{\max} changes with z_{\max} and has a maximum value near $z_{\max} = 0.30$. The average error and D_{\max} increase as the used number of SNe decreases. Comparing with the previous researches, we find all preferred directions we obtained are in line with that were provided by Antoniou & Perivolaropoulos (2010), Cai & Tuo (2012), Wang & Wang (2014), Yang et al. (2014), Kalus et al. (2013), Chang & Lin (2015), Lin et al. (2016b), Chang & Zhou (2019), and Hu et al. (2020), but they are not consistent with those given by Luongo et al. (2022) and McConville & Colgáin (2023).

Until now, many SNe Ia have been observed and have been widely used for cosmological applications (Hoscheit & Barger 2018; Perivolaropoulos & Skara 2021; Cowell et al. 2023; Hu & Wang 2022a; Wang 2022; Briffa et al. 2023).⁴ However, there is still an inhomogeneous distribution in data, which significantly affects the testing of cosmological principle. One way to solve this problem is to add some new SNe Ia measurements, and another way is to consider other independent observations; for example, quasar (Lusso & Risaliti 2016; Bisogni et al. 2017; Lusso & Risaliti 2017; Risaliti & Lusso 2019; Cao et al. 2022b; Khadka et al. 2022; Liu et al. 2023a; Zajaček et al. 2023), gamma-ray burst (GRB; Wang et al. 2015; Shirokov et al. 2020; Hu et al. 2021; Cao et al. 2022a; Liu et al. 2022b; Lovyagin et al. 2022; Liang et al. 2022; Wang et al. 2022), fast radio burst (FRB; Hagstotz et al. 2022; Wu et al. 2022; James et al. 2022; Zhao et al. 2022; Gao et al. 2023; Liu et al. 2023b), Tip of the Red Giant Branch (TRGB; Freedman et al. 2019, 2020; Freedman 2021), galaxy cluster (Javanmardi & Kroupa 2017; Migkas et al. 2020, 2021), and gravitational wave (GW; Abbott et al. 2017; Chen et al. 2018; Jin et al. 2023; Wang et al. 2023b) observations, among others. At present, these observations may still have some deficiencies in quantity or quality, but this situation is expected to improve in the future. The e-RSITA all-sky survey (Merloni et al. 2012; Predehl 2012; Kolodzig et al. 2013; Lusso 2020), Einstein Probe (EP; Yuan et al. 2015), French-

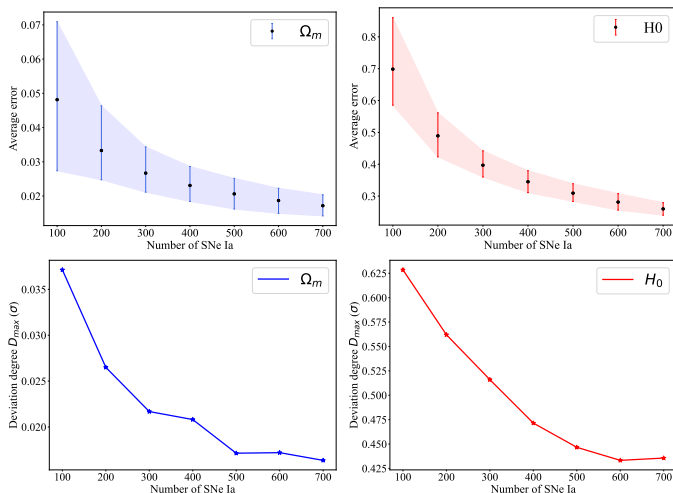


Fig. 17. Relationship between average error and discrepancy degree D_{\max} and SN number used. The upper panels show the relationship between the average error and the used SN number. The lower panels show the relationship between the discrepancy degree D_{\max} and the SN number used. Blue and red correspond to parameters Ω_m and H_0 , respectively.

⁴ For more recent studies on the cosmological applications employing the SNe Ia sample, see Bargiacchi et al. (2023), Cao & Ratra (2023), de Jaeger & Galbany (2023), Hu et al. (2023), Jin et al. (2023), Kumar et al. (2023), Lapi et al. (2023), Mandal et al. (2023), Ó Colgáin et al. (2023), Pastén & Cárdenas (2023), Perivolaropoulos & Skara (2023), Sakr (2023), Van Raamsdonk & Waddell (2023), Wang et al. (2023a), and references therein.

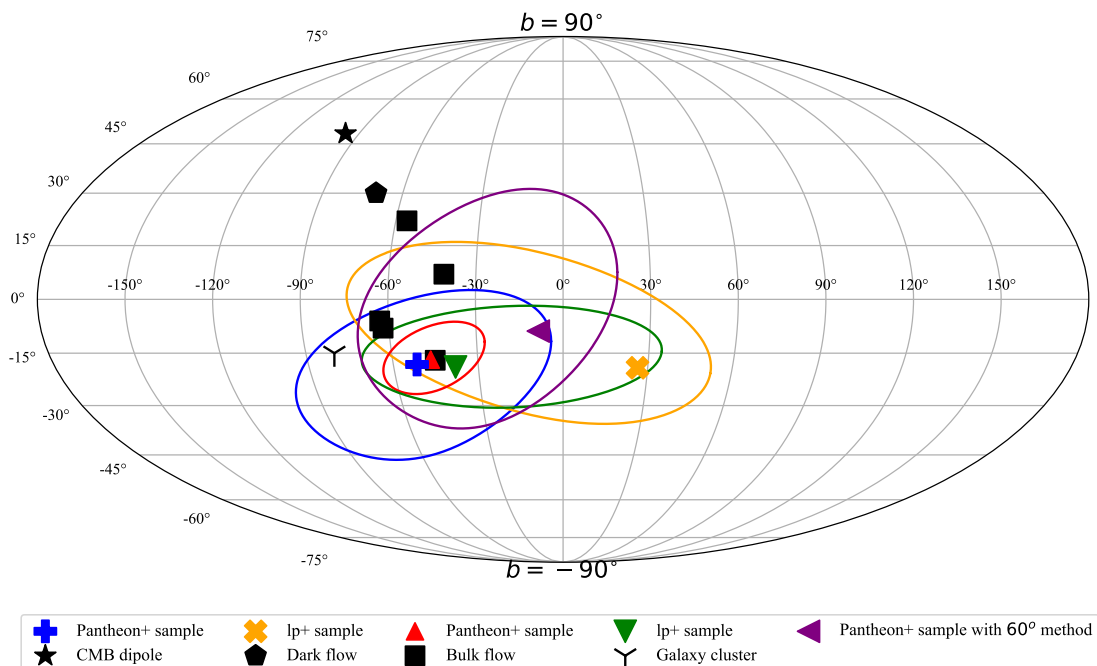


Fig. 18. Distribution of preferred directions (l, b) with 1σ range in other independent observations. We mark the directions given by Ω_m with plus signs at different screening angles, and the directions given by H_0 are shown with triangles at different screening angles. The color represents the important result obtained in this work; black shows the result given by other independent observations including the CMB dipole (Planck Collaboration et al. 2016, 2020a), dark flow (Abdalla et al. 2022), bulk flow (Turnbull et al. 2012; Feix et al. 2017; Watkins et al. 2023), and galaxy cluster (Migkas et al. 2021).

Table 3. Preferred directions given by other independent observations.

Cosmological obs.	Direction (l, b)	Ref.
CMB dipole	$(264.00^\circ \pm 0.03, 48.24^\circ \pm 0.02)$	(Planck Collaboration et al. 2016)
	$(264.02^\circ \pm 0.01, 48.25^\circ \pm 0.01)$	(Planck Collaboration et al. 2020a)
Dark flow	$(290^\circ \pm 20, 30^\circ \pm 15)$	(Abdalla et al. 2022)
Bulk flow	$(319^\circ \pm 18, 7^\circ \pm 14)$	(Turnbull et al. 2012)
	$(315^\circ \pm 52, -17^\circ \pm 15)$	(Feix et al. 2017)
	$(304^\circ \pm 14, 22^\circ \pm 11)$	(Feix et al. 2017)
	$(297^\circ \pm 4, -6^\circ \pm 3)$	(Watkins et al. 2023)
	$(298^\circ \pm 5, -8^\circ \pm 4)$	(Watkins et al. 2023)
Galaxy cluster	$(280^\circ \pm 35, -15^\circ \pm 20)$	(Migkas et al. 2021)
Pantheon+ ($H_0, 90^\circ$)	$(313.4^\circ_{-18.2}^{+19.6}, -16.8^\circ_{-10.7}^{+11.1})$	this paper
Pantheon+ ($H_0, 60^\circ$)	$(351.4^\circ_{-64.2}^{+28.0}, -8.8^\circ_{-27.8}^{+40.3})$	this paper
Ip+ ($H_0, 90^\circ$)	$(321.9^\circ_{-33.5}^{+72.5}, -18.9^\circ_{-11.5}^{+16.6})$	this paper
Pantheon+ ($\Omega_m, 90^\circ$)	$(308.4^\circ_{-48.7}^{+47.6}, -18.2^\circ_{-28.8}^{+21.1})$	this paper
Ip+ ($\Omega_m, 90^\circ$)	$(26.4^\circ_{-100.9}^{+26.3}, -19.3^\circ_{-17.0}^{+35.4})$	this paper

Chinese satellite space-based multi-band astronomical variable objects monitor (SVOM; Wei et al. 2016), China Space Station Telescope (CSST) photometric survey (Xu et al. 2022; Miao et al. 2023; Li et al. 2023a), and Transient High-Energy Sky and Early Universe Surveyor (THESEUS; Amati et al. 2018) space missions together with ground- and space-based multi-messenger facilities will provide a lot of observations and measurements, improve the observational quality, and probe the poorly explored high-redshift universe. The Australian Square Kilometer Array Pathfinder (ASKAP; Chapman et al. 2017), MeerKAT (Sanidas et al. 2018), Very Large Array (VLA; Law et al. 2018), and Canadian Hydrogen Intensity Mapping Experiment (CHIME)/FRB Outriggers (Leung et al. 2021) will provide a large number of positioned FRBs in the future, which will

give higher precision cosmological constraints. In addition, the Advanced Laser Interferometer Gravitational-wave Observatory (aLIGO; LIGO Scientific Collaboration et al. 2015) and Virgo (Acernese et al. 2015) detectors will provide more GW events. In combination with the electromagnetic counterparts, model-independent constraints will be given on the cosmological parameters. The high-quality observations enable us to examine the cosmological principle at higher redshifts and investigate whether the Hubble tension is related to the failure of the cosmological principle.

Notes: As this work was about to be completed, Perivolaropoulos (2023) used the HC method to test the cosmic isotropy of the SNe Ia absolute magnitudes from the Pantheon+ and SH0ES samples in various redshift/distance bins. They found that sharp

changes of the level of anisotropy occurring at distances under 40 Mpc in the real samples. If there are enough local observations in the future, more local information about our Universe could be obtained by combining our method with the idea of Perivolaropoulos (2023). This will be pursued in future work.

Acknowledgements

We thank the anonymous referee for constructive comments. This work was supported by the National Natural Science Foundation of China (grant No. 12273009), the China Manned Space Project (CMS-CSST-2021-A12), Jiangsu Funding Program for Excellent Postdoctoral Talent (20220ZB59), Project funded by China Postdoctoral Science Foundation (2022M721561), NWO, the Dutch Research Council, under Vici research programme ‘ARGO’ with project number 639.043.815, Yunnan Youth Basic Research Projects 202001AU070013 and National Natural Science Foundation of China (grant No. 12303050).

References

- Abbott, B. P., Abbott, R., Abbott, T. D., et al. 2017, *Nature*, 551, 85
- Abbott, T. M. C., Alarcon, A., Allam, S., et al. 2019, *Phys. Rev. Lett.*, 122, 171301
- Abdalla, E., Abellán, G. F., Aboubrahim, A., et al. 2022, *Journal of High Energy Astrophysics*, 34, 49
- Acernese, F., Agathos, M., Agatsuma, K., et al. 2015, *Classical and Quantum Gravity*, 32, 024001
- Akarsu, Ö., Barrow, J. D., & Uzun, N. M. 2020, *Phys. Rev. D*, 102, 124059
- Akarsu, O., Dereli, T., & Katurci, N. 2022, in *Journal of Physics Conference Series*, Vol. 2191, *Journal of Physics Conference Series*, 012001
- Akarsu, Ö., Di Valentino, E., Kumar, S., Özyigit, M., & Sharma, S. 2023, *Physics of the Dark Universe*, 39, 101162
- Amati, L., O’Brien, P., Götz, D., et al. 2018, *Advances in Space Research*, 62, 191
- Andrade, U., Bengaly, C. A. P., Santos, B., & Alcaniz, J. S. 2018, *ApJ*, 865, 119
- Antoniu, I. & Perivolaropoulos, L. 2010, *J. Cosmology Astropart. Phys.*, 2010, 012
- Bargiacchi, G., Dainotti, M. G., Nagataki, S., & Capozziello, S. 2023, *MNRAS*, 521, 3909
- Bayron Orjuela-Quintana, J., Álvarez, M., Valenzuela-Toledo, C. A., & Rodríguez, Y. 2020, *J. Cosmology Astropart. Phys.*, 2020, 019
- Bennett, C. L., Halpern, M., Hinshaw, G., et al. 2003, *ApJS*, 148, 1
- Bennett, C. L., Hill, R. S., Hinshaw, G., et al. 2011, *ApJS*, 192, 17
- Bennett, C. L., Larson, D., Weiland, J. L., et al. 2013, *ApJS*, 208, 20
- Betoule, M., Kessler, R., Guy, J., et al. 2014, *A&A*, 568, A22
- Bielewicz, P., Górski, K. M., & Banday, A. J. 2004, *MNRAS*, 355, 1283
- Bisogni, S., Risaliti, G., & Lusso, E. 2017, *Frontiers in Astronomy and Space Sciences*, 4, 68
- Böhringer, H., Chon, G., & Collins, C. A. 2020, *A&A*, 633, A19
- Bonvin, C., Durrer, R., & Kunz, M. 2006, *Phys. Rev. Lett.*, 96, 191302
- Briffa, R., Escamilla-Rivera, C., Said, J. L., & Mifsud, J. 2023, *MNRAS*, 522, 6024
- Brout, D., Sako, M., Scolnic, D., et al. 2019, *ApJ*, 874, 106
- Brout, D., Scolnic, D., Popovic, B., et al. 2022, *ApJ*, 938, 110
- Brown, P. J., Breeveld, A. A., Holland, S., Kuin, P., & Pritchard, T. 2014, *Ap&SS*, 354, 89
- Cai, R.-G., Ding, J.-F., Guo, Z.-K., Wang, S.-J., & Yu, W.-W. 2021, *Phys. Rev. D*, 103, 123539
- Cai, R.-G. & Tuo, Z.-L. 2012, *J. Cosmology Astropart. Phys.*, 2012, 004
- Cai, T., Ding, Q., & Wang, Y. 2022, arXiv e-prints, arXiv:2211.06857
- Camarena, D., Marra, V., Sakr, Z., & Clarkson, C. 2022, *Classical and Quantum Gravity*, 39, 184001
- Cao, S., Khadka, N., & Ratra, B. 2022a, *MNRAS*, 510, 2928
- Cao, S. & Ratra, B. 2022, *MNRAS*, 513, 5686
- Cao, S. & Ratra, B. 2023, *Phys. Rev. D*, 107, 103521
- Cao, S., Zajaček, M., Panda, S., et al. 2022b, *MNRAS*, 516, 1721
- Capozziello, S., Sarracino, G., & Spallicci, A. D. A. M. 2023, *Physics of the Dark Universe*, 40, 101201
- Carr, A., Davis, T. M., Scolnic, D., et al. 2022, *PASA*, 39, e046
- Castello, S., Högås, M., & Mörtzell, E. 2022, *J. Cosmology Astropart. Phys.*, 2022, 003
- Chang, Z. & Lin, H.-N. 2015, *MNRAS*, 446, 2952
- Chang, Z., Lin, H.-N., Zhao, Z.-C., & Zhou, Y. 2018, *Chinese Physics C*, 42, 115103
- Chang, Z. & Zhou, Y. 2019, *MNRAS*, 486, 1658
- Chapman, J. M., Dempsey, J., Miller, D., et al. 2017, in *Astronomical Society of the Pacific Conference Series*, Vol. 512, *Astronomical Data Analysis Software and Systems XXV*, ed. N. P. F. Lorente, K. Shorridge, & R. Wayth, 73
- Chen, H.-Y. 2019, *Nature Astronomy*, 3, 384
- Chen, H.-Y., Fishbach, M., & Holz, D. E. 2018, *Nature*, 562, 545
- Colgáin, E. O., Sheikh-Jabbari, M. M., Solomon, R., Dainotti, M. G., & Stojkovic, D. 2022, arXiv e-prints, arXiv:2206.11447
- Colin, J., Mohayaee, R., Rameez, M., & Sarkar, S. 2017, *MNRAS*, 471, 1045
- Colin, J., Mohayaee, R., Rameez, M., & Sarkar, S. 2019, *A&A*, 631, L13
- Colin, J., Mohayaee, R., Sarkar, S., & Shafieloo, A. 2011, *MNRAS*, 414, 264
- Cowell, J. A., Dhawan, S., & Macpherson, H. J. 2023, *MNRAS*, 526, 1482
- Dainotti, M. G., De Simone, B., Schiavone, T., et al. 2021, *ApJ*, 912, 150
- Dainotti, M. G., De Simone, B. D., Schiavone, T., et al. 2022a, *Galaxies*, 10, 24
- Dainotti, M. G., Nielson, V., Sarracino, G., et al. 2022b, *MNRAS*, 514, 1828
- Dam, L., Lewis, G. F., & Brewer, B. J. 2023, *MNRAS*, 525, 231
- Davis, T. M., Hui, L., Frieman, J. A., et al. 2011, *ApJ*, 741, 67
- de Cruz Pérez, J., Park, C.-G., & Ratra, B. 2023, *Phys. Rev. D*, 107, 063522
- de Jaeger, T. & Galbany, L. 2023, arXiv e-prints, arXiv:2305.17243
- Deng, H.-K. & Wei, H. 2018a, *European Physical Journal C*, 78, 755
- Deng, H.-K. & Wei, H. 2018b, *Phys. Rev. D*, 97, 123515
- Dhawan, S., Borderies, A., Macpherson, H. J., & Heinesen, A. 2023, *MNRAS*, 519, 4841
- Di Valentino, E., Mena, O., Pan, S., et al. 2021, *Classical and Quantum Gravity*, 38, 153001
- Ebrahimian, E., Krishnan, C., Mondol, R., & Sheikh-Jabbari, M. M. 2023, arXiv e-prints, arXiv:2305.16177
- Enqvist, K. 2008, *General Relativity and Gravitation*, 40, 451
- Feix, M., Branchini, E., & Nusser, A. 2017, *MNRAS*, 468, 1420
- Ferreira, P. d. S. & Quartin, M. 2021, *Phys. Rev. D*, 104, 063503
- Foley, R. J., Scolnic, D., Rest, A., et al. 2018, *MNRAS*, 475, 193
- Foreman-Mackey, D., Hogg, D. W., Lang, D., & Goodman, J. 2013, *PASP*, 125, 306
- Freedman, W. L. 2021, *ApJ*, 919, 16
- Freedman, W. L., Madore, B. F., Hatt, D., et al. 2019, *ApJ*, 882, 34
- Freedman, W. L., Madore, B. F., Hoyt, T., et al. 2020, *ApJ*, 891, 57
- Ganeshalingam, M., Li, W., Filippenko, A. V., et al. 2010, *ApJS*, 190, 418
- Gao, J., Zhou, Z., Du, M., et al. 2023, arXiv e-prints, arXiv:2307.08285
- García-Bellido, J. & Haugbølle, T. 2008, *J. Cosmology Astropart. Phys.*, 2008, 003
- Ghosh, S. & Jain, P. 2020, *MNRAS*, 492, 3994
- Ghosh, S., Kothari, R., Jain, P., & Rath, P. K. 2016, *J. Cosmology Astropart. Phys.*, 2016, 046
- Gruppuso, A., Finelli, F., Natoli, P., et al. 2011, *MNRAS*, 411, 1445
- Gurzadyan, V. G., Fimin, N. N., & Chechetkin, V. M. 2023, *A&A*, 677, A161
- Haagstotz, S., Reischke, R., & Lilow, R. 2022, *MNRAS*, 511, 662
- Hamaus, N., Aubert, M., Pisani, A., et al. 2022, *A&A*, 658, A20
- Hansen, F. K., Banday, A. J., & Górski, K. M. 2004, *MNRAS*, 354, 641
- Haslbauer, M., Banik, I., & Kroupa, P. 2020, *MNRAS*, 499, 2845
- Horstmann, N., Pietschke, Y., & Schwarz, D. J. 2022, *A&A*, 668, A34
- Hoscheit, B. L. & Barger, A. J. 2018, *ApJ*, 854, 46
- Hu, J., Hu, J.-P., Li, Z., Zhao, W., & Chen, J. 2023, *Phys. Rev. D*, 108, 083024
- Hu, J. P. & Wang, F. Y. 2022a, *A&A*, 661, A71
- Hu, J. P. & Wang, F. Y. 2022b, *MNRAS*, 517, 576
- Hu, J.-P. & Wang, F.-Y. 2023, *Universe*, 9, 94
- Hu, J. P., Wang, F. Y., & Dai, Z. G. 2021, *MNRAS*, 507, 730
- Hu, J. P., Wang, Y. Y., & Wang, F. Y. 2020, *A&A*, 643, A93
- Hui, L. & Greene, P. B. 2006, *Phys. Rev. D*, 73, 123526
- Hutsemékers, D., Cabanac, R., Lamy, H., & Sluse, D. 2005, *A&A*, 441, 915
- Hwang, H. S., Geller, M. J., Park, C., et al. 2016, *ApJ*, 818, 173
- James, C. W., Ghosh, E. M., Prochaska, J. X., et al. 2022, *MNRAS*, 516, 4862
- Javanmardi, B. & Kroupa, P. 2017, *A&A*, 597, A120
- Javanmardi, B., Porciani, C., Kroupa, P., & Pflamm-Altenburg, J. 2015, *ApJ*, 810, 47
- Jia, X. D., Hu, J. P., & Wang, F. Y. 2023, *A&A*, 674, A45
- Jia, X. D., Hu, J. P., Yang, J., Zhang, B. B., & Wang, F. Y. 2022, *MNRAS*, 516, 2575
- Jin, S.-J., Xing, S.-S., Shao, Y., Zhang, J.-F., & Zhang, X. 2023, *Chinese Physics C*, 47, 065104
- Kalbounch, B., Marinoni, C., & Bel, J. 2023, *Phys. Rev. D*, 107, 023507
- Kalus, B., Schwarz, D. J., Seikel, M., & Wiegand, A. 2013, *A&A*, 553, A56
- Kazantzidis, L. & Perivolaropoulos, L. 2020, *Phys. Rev. D*, 102, 023520
- Keenan, R. C., Barger, A. J., & Cowie, L. L. 2013, *ApJ*, 775, 62
- Kelly, P. L., Rodney, S., Treu, T., et al. 2023, *Science*, 380, abh1322
- Kelly, P. L., Rodney, S. A., Treu, T., et al. 2015, *Science*, 347, 1123
- Kenworthy, W. D., Scolnic, D., & Riess, A. 2019, *ApJ*, 875, 145
- Khadka, N. & Ratra, B. 2020, *MNRAS*, 492, 4456

- Khadka, N., Zajaček, M., Panda, S., Martínez-Aldama, M. L., & Ratra, B. 2022, *MNRAS*, 515, 3729
- Khadka, N., Zajaček, M., Prince, R., et al. 2023, *MNRAS*, 522, 1247
- King, J. A., Webb, J. K., Murphy, M. T., et al. 2012, *MNRAS*, 422, 3370
- Koivisto, T. & Mota, D. F. 2008, *J. Cosmology Astropart. Phys.*, 2008, 018
- Koksbang, S. M. 2021, *Phys. Rev. Lett.*, 126, 231101
- Kolodzig, A., Gilfanov, M., Sunyaev, R., Sazonov, S., & Brusa, M. 2013, *A&A*, 558, A89
- Krishnan, C., Colgáin, E. Ó., Ruchika, Sen, A. A., Sheikh-Jabbari, M. M., & Yang, T. 2020, *Phys. Rev. D*, 102, 103525
- Krishnan, C., Mohayaee, R., Colgáin, E. Ó., Sheikh-Jabbari, M. M., & Yin, L. 2021a, *Classical and Quantum Gravity*, 38, 184001
- Krishnan, C., Mohayaee, R., Colgáin, E. Ó., Sheikh-Jabbari, M. M., & Yin, L. 2022, *Phys. Rev. D*, 105, 063514
- Krishnan, C., Ó Colgáin, E., Sheikh-Jabbari, M. M., & Yang, T. 2021b, *Phys. Rev. D*, 103, 103509
- Kroupa, P., Gjergo, E., Asencio, E., et al. 2023, arXiv e-prints, arXiv:2309.11552
- Kumar, D., Choudhury, D., & Nandi, D. 2023, arXiv e-prints, arXiv:2310.03509
- Kumar Aluri, P., Cea, P., Chingangbam, P., et al. 2023, *Classical and Quantum Gravity*, 40, 094001
- Lapi, A., Boco, L., Cueli, M. M., et al. 2023, arXiv e-prints, arXiv:2310.06028
- Law, C. J., Bower, G. C., Burke-Spolaor, S., et al. 2018, *ApJS*, 236, 8
- Leung, C., Mena-Parra, J., Masui, K., et al. 2021, *AJ*, 161, 81
- Lewis, A. 2019, arXiv e-prints, arXiv:1910.13970
- Li, S.-Y., Li, Y.-L., Zhang, T., et al. 2023a, *Science China Physics, Mechanics, and Astronomy*, 66, 229511
- Li, X. & Lin, H.-N. 2017, *Chinese Physics C*, 41, 065102
- Li, Z., Zhang, B., & Liang, N. 2023b, *MNRAS*, 521, 4406
- Liang, N., Li, Z., Xie, X., & Wu, P. 2022, *ApJ*, 941, 84
- LIGO Scientific Collaboration, Aasi, J., Abbott, B. P., et al. 2015, *Classical and Quantum Gravity*, 32, 074001
- Lin, H.-N., Li, X., & Chang, Z. 2016a, *MNRAS*, 460, 617
- Lin, H.-N., Wang, S., Chang, Z., & Li, X. 2016b, *MNRAS*, 456, 1881
- Liu, T., Yang, X., Zhang, Z., Wang, J., & Biesiada, M. 2023a, *Physics Letters B*, 845, 138166
- Liu, Y., Chen, F., Liang, N., et al. 2022a, *ApJ*, 931, 50
- Liu, Y., Liang, N., Xie, X., et al. 2022b, *ApJ*, 935, 7
- Liu, Y., Yu, H., & Wu, P. 2023b, *ApJ*, 946, L49
- Lovaygin, N. Y., Gairnutdinov, R. I., Shirokov, S. I., & Gorokhov, V. L. 2022, *Universe*, 8, 344
- Luković, V. V., Haridasu, B. S., & Vittorio, N. 2020, *MNRAS*, 491, 2075
- Luongo, O., Muccino, M., Colgáin, E. Ó., Sheikh-Jabbari, M. M., & Yin, L. 2022, *Phys. Rev. D*, 105, 103510
- Lusso, E. 2020, *Frontiers in Astronomy and Space Sciences*, 7, 8
- Lusso, E. & Risaliti, G. 2016, *ApJ*, 819, 154
- Lusso, E. & Risaliti, G. 2017, *A&A*, 602, A79
- Malekjani, M., Mc Conville, R., Colgáin, E. Ó., Pourojaghi, S., & Sheikh-Jabbari, M. M. 2023, arXiv e-prints, arXiv:2301.12725
- Mandal, S., Duffell, P. C., Polin, A., & Milisavljevic, D. 2023, *ApJ*, 956, 130
- Mariano, A. & Perivolaropoulos, L. 2012, *Phys. Rev. D*, 86, 083517
- McConville, R. & Colgáin, E. Ó. 2023, arXiv e-prints, arXiv:2304.02718
- Merloni, A., Predehl, P., Becker, W., et al. 2012, arXiv e-prints, arXiv:1209.3114
- Miao, H., Gong, Y., Chen, X., et al. 2023, *MNRAS*, 519, 1132
- Migkas, K., Pacaud, F., Schellenberger, G., et al. 2021, *A&A*, 649, A151
- Migkas, K., Schellenberger, G., Reiprich, T. H., et al. 2020, *A&A*, 636, A15
- Milaković, D., Lee, C.-C., Molaro, P., & Webb, J. K. 2022, arXiv e-prints, arXiv:2212.02458
- Millon, M., Galan, A., Courbin, F., et al. 2020, *A&A*, 639, A101
- Mohammadi, S., Yusofi, E., Mohsenzadeh, M., & Salem, M. K. 2023, *MNRAS*, 525, 3274
- Motoa-Manzano, J., Orjuela-Quintana, J. B., Pereira, T. S., & Valenzuela-Toledo, C. A. 2021, *Physics of the Dark Universe*, 32, 100806
- Ó Colgáin, E., Sheikh-Jabbari, M. M., & Solomon, R. 2023, *Physics of the Dark Universe*, 40, 101216
- Ó Colgáin, E., Sheikh-Jabbari, M. M., Solomon, R., et al. 2022, *Phys. Rev. D*, 106, L041301
- Pandey, B. 2017, *MNRAS*, 468, 1953
- Pastén, E. & Cárdenas, V. H. 2023, *Physics of the Dark Universe*, 40, 101224
- Pedregosa, F., Varoquaux, G., Gramfort, A., et al. 2011, *Journal of Machine Learning Research*, 12, 2825
- Pelgrims, V. & Hutsemékers, D. 2016, *A&A*, 590, A53
- Perivolaropoulos, L. 2023, *Phys. Rev. D*, 108, 063509
- Perivolaropoulos, L. & Skara, F. 2021, *Phys. Rev. D*, 104, 123511
- Perivolaropoulos, L. & Skara, F. 2022, *New A Rev.*, 95, 101659
- Perivolaropoulos, L. & Skara, F. 2023, *MNRAS*, 520, 5110
- Planck Collaboration, Adam, R., Ade, P. A. R., et al. 2016, *A&A*, 594, A1
- Planck Collaboration, Aghanim, N., Akrami, Y., et al. 2020a, *A&A*, 641, A1
- Planck Collaboration, Aghanim, N., Akrami, Y., et al. 2020b, *A&A*, 641, A6
- Planck Collaboration, Akrami, Y., Ashdown, M., et al. 2020c, *A&A*, 641, A7
- Porredon, A., Crocce, M., Elvin-Poole, J., et al. 2022, *Phys. Rev. D*, 106, 103530
- Predehl, P. 2012, in *Society of Photo-Optical Instrumentation Engineers (SPIE) Conference Series*, Vol. 8443, *Space Telescopes and Instrumentation 2012: Ultraviolet to Gamma Ray*, ed. T. Takahashi, S. S. Murray, & J.-W. A. den Herder, 84431R
- Rahman, W., Trotta, R., Boruah, S. S., Hudson, M. J., & van Dyk, D. A. 2022, *MNRAS*, 514, 139
- Rameez, M., Mohayaee, R., Sarkar, S., & Colin, J. 2018, *MNRAS*, 477, 1772
- Refsdal, S. 1964, *MNRAS*, 128, 295
- Riess, A. G. 2020, *Nature Reviews Physics*, 2, 10
- Riess, A. G. & Breuval, L. 2023, arXiv e-prints, arXiv:2308.10954
- Riess, A. G., Casertano, S., Yuan, W., Macri, L. M., & Scolnic, D. 2019, *ApJ*, 876, 85
- Riess, A. G., Yuan, W., Macri, L. M., et al. 2022, *ApJ*, 934, L7
- Risaliti, G. & Lusso, E. 2019, *Nature Astronomy*, 3, 272
- Rubart, M., Bacon, D., & Schwarz, D. J. 2014, *A&A*, 565, A111
- Sakr, Z. 2023, *Phys. Rev. D*, 108, 083519
- Sanidas, S., Caleb, M., Driessen, L., et al. 2018, in *Pulsar Astrophysics the Next Fifty Years*, ed. P. Weltevrede, B. B. P. Perera, L. L. Preston, & S. Sanidas, Vol. 337, 406–407
- Schwarz, D. J. & Weinhorst, B. 2007, *A&A*, 474, 717
- Scolnic, D., Brout, D., Carr, A., et al. 2022, *ApJ*, 938, 113
- Scolnic, D. M., Jones, D. O., Rest, A., et al. 2018, *ApJ*, 859, 101
- Secrest, N. J., von Hausegger, S., Rameez, M., et al. 2021, *ApJ*, 908, L51
- Shah, P., Lemos, P., & Lahav, O. 2021, *A&A Rev.*, 29, 9
- Shim, J., Park, C., Kim, J., & Hong, S. E. 2023, *ApJ*, 952, 59
- Shirokov, S. I., Sokolov, I. V., Lovaygin, N. Y., et al. 2020, *MNRAS*, 496, 1530
- Singal, A. K. 2019, *Phys. Rev. D*, 100, 063501
- Singal, A. K. 2023, *MNRAS*, 524, 3636
- Smith, M., D'Andrea, C. B., Sullivan, M., et al. 2020, *AJ*, 160, 267
- Stahl, B. E., Zheng, W., de Jaeger, T., et al. 2019, *MNRAS*, 490, 3882
- Sun, Z. Q. & Wang, F. Y. 2018, *MNRAS*, 478, 5153
- Sun, Z. Q. & Wang, F. Y. 2019, *European Physical Journal C*, 79, 783
- Tang, L., Lin, H.-N., Liu, L., & Li, X. 2023, *Chinese Physics C*, 47, 125101
- Tegmark, M., de Oliveira-Costa, A., & Hamilton, A. J. 2003, *Phys. Rev. D*, 68, 123523
- Tiwari, P. & Jain, P. 2019, *A&A*, 622, A113
- Tripp, R. 1998, *A&A*, 331, 815
- Turnbull, S. J., Hudson, M. J., Feldman, H. A., et al. 2012, *MNRAS*, 420, 447
- Vagnozzi, S. 2023, *Universe*, 9, 393
- Van Raamsdonk, M. & Waddell, C. 2023, arXiv e-prints, arXiv:2305.04946
- Verde, L., Treu, T., & Riess, A. G. 2019, *Nature Astronomy*, 3, 891
- Wang, D. 2022, *Phys. Rev. D*, 106, 063515
- Wang, F. Y. & Dai, Z. G. 2013, *MNRAS*, 432, 3025
- Wang, F. Y., Dai, Z. G., & Liang, E. W. 2015, *New A Rev.*, 67, 1
- Wang, F. Y., Hu, J. P., Zhang, G. Q., & Dai, Z. G. 2022, *ApJ*, 924, 97
- Wang, J. S. & Wang, F. Y. 2014, *MNRAS*, 443, 1680
- Wang, K., Chen, K.-P., & Le Delliou, M. 2023a, *European Physical Journal C*, 83, 859
- Wang, Y.-Y., Tang, S.-P., Jin, Z.-P., & Fan, Y.-Z. 2023b, *ApJ*, 943, 13
- Wang, Y.-Y. & Wang, F. Y. 2018, *MNRAS*, 474, 3516
- Watkins, R., Allen, T., Bradford, C. J., et al. 2023, *MNRAS*, 524, 1885
- Webb, J. K., King, J. A., Murphy, M. T., et al. 2011, *Phys. Rev. Lett.*, 107, 191101
- Wei, J., Cordier, B., Antier, S., et al. 2016, arXiv e-prints, arXiv:1610.06892
- Wong, K. C., Suyu, S. H., Chen, G. C. F., et al. 2020, *MNRAS*, 498, 1420
- Wu, Q., Zhang, G.-Q., & Wang, F.-Y. 2022, *MNRAS*, 515, L1
- Xu, Y.-T., Dai, J.-P., Zhao, D., & Xia, J.-Q. 2022, *MNRAS*, 515, 5587
- Yang, X., Wang, F. Y., & Chu, Z. 2014, *MNRAS*, 437, 1840
- Yuan, W., Zhang, C., Feng, H., et al. 2015, arXiv e-prints, arXiv:1506.07735
- Zajaček, M., Czerny, B., Khadka, N., et al. 2023, arXiv e-prints, arXiv:2305.08179
- Zhao, D. & Xia, J.-Q. 2021a, *European Physical Journal C*, 81, 948
- Zhao, D. & Xia, J.-Q. 2021b, *European Physical Journal C*, 81, 694
- Zhao, D. & Xia, J.-Q. 2022, *MNRAS*, 511, 5661
- Zhao, D., Zhou, Y., & Chang, Z. 2019, *MNRAS*, 486, 5679
- Zhao, Z.-W., Zhang, J.-G., Li, Y., et al. 2022, arXiv e-prints, arXiv:2212.13433
- Zhou, Y., Zhao, Z.-C., & Chang, Z. 2017, *ApJ*, 847, 86

Appendix A: Additional figures

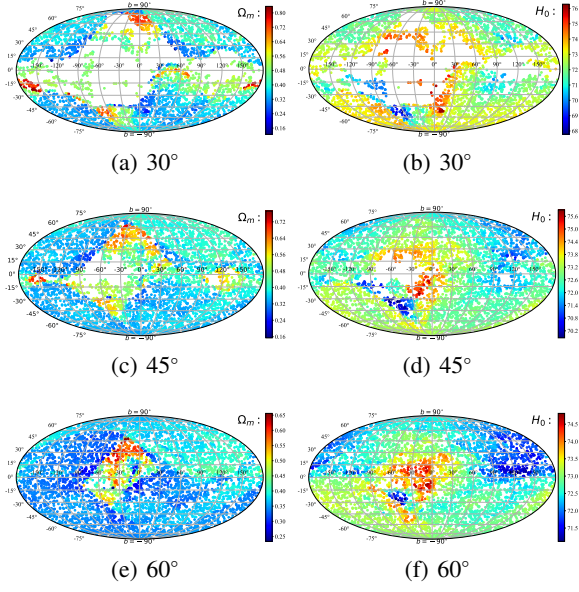


Fig. A.1. All-sky distribution of cosmological parameter (Ω_m and H_0) utilizing the Pantheon+ sample combined with the RF method with different screening angles including 30° , 45° , and 60° . Panels (a) and (b) show the results using the RF method with 30° . Panels (c) and (d) are the results of 45° . Panels (e) and (f) are the results of 60° . The proportions of the wrong fitting results are 30.34%, 6.47%, and 0.70% for the screening angles 30° , 45° , and 60° , respectively.

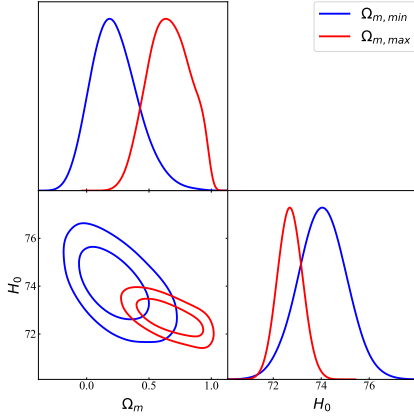


Fig. A.2. Confidence contours (1σ and 2σ) and marginalized likelihood distributions for parameters space (Ω_m and H_0) in the spatially flat Λ CDM model from SNe Ia subsamples, which corresponds to $\Omega_{m,min}$ and $\Omega_{m,max}$. The best fits are $\Omega_{m,min} = 0.23^{+0.20}_{-0.17}$ and $H_0 = 74.05^{+1.00}_{-1.00}$ km s $^{-1}$ Mpc $^{-1}$ and $\Omega_{m,max} = 0.66^{+0.17}_{-0.17}$ and $H_0 = 72.70^{+0.52}_{-0.52}$ km s $^{-1}$ Mpc $^{-1}$.